

270260-2-F

Analysis of Pupil Plane Target Characterization Experiments

Final Report

APRIL 1998

J.R. Fienup, C.C. Aleksoff, and T.J. Schulz

Prepared for:

Dr. Guy Beaghler

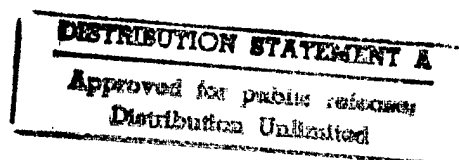
NCCOSC

NRaD, Code 804

53570 Silvergate Ave., Rm. 2070

San Diego, CA 92152-5070

Contract No. N-62269-91-C-0526



19980624 106



P.O. Box 134008 Ann Arbor, MI 48113-4008 734-994-1200

<http://www.irim-int.com>

DTIC QUALITY INSPECTED 1

ERIM-320		REPORT DOCUMENTATION PAGE Form Approved OMB No. 0704-0188	
Public reporting burden for the collection of information is estimated to average 1 hour per response, including the time for reviewing instructions, searching existing data sources, gathering and maintaining the data needed, and completing and reviewing the collection of information. Send comments regarding this burden estimate or any other aspect of this collection of information, including suggestions for reducing this burden, to Washington Headquarters Services, Directorate for Information Operations and Reports, 1215 Jefferson Davis Highway, Suite 1204, Arlington, VA 22202-4302, and to the Office of Management and Budget, Paperwork Reduction Project (0704-0188), Washington, DC 20503.			
1. AGENCY USE ONLY (Leave Blank)	2. REPORT DATE April 1998	3. REPORT TYPE AND DATES COVERED Final, April 1998	
4. TITLE AND SUBTITLE Analysis of Pupil Plane Target Characterization Experiments		5. FUNDING NUMBERS N-62269-91-C-0526	
6. AUTHOR(s) J.R. Fienup, C.C. Aleksoff, and T.J. Schulz			
7. PERFORMING ORGANIZATION NAMES(s) AND ADDRESS(es) ERIM International, Inc. P.O. Box 134008 Ann Arbor, MI 48113-4008		8. PERFORMING ORGANIZATION REPORT NUMBER ERIM 270260-2-F	
9. SPONSORING/MONITORING AGENCY NAME(s) AND ADDRESS(es) Naval Air Warfare Center (NAWC)/Aircraft Division/Patuxent River Code 4.5.5.5, bldg. 2187, Suite 2190-G1 22347 Cedar Point Road Patuxent River, MD 20670-1161		10. SPONSORING/MONITORING AGENCY REPORT NUMBER	
11. SUPPLEMENTARY NOTES			
12a. DISTRIBUTION/AVAILABILITY STATEMENT Approved for public release; distribution unlimited		12b. DISTRIBUTION CODE	
13. ABSTRACT (Maximum of 200 Words) We investigated approaches for gathering information about a missile at long ranges employing flood-illumination by a laser and pupil-plane arrays of detectors. We catalogued target parameters that could be characterized with these measurements. We showed the ability to estimate the length, width, and orientation of the missile from pupil-plane speckle patterns. We demonstrated shape reconstruction from the autocorrelation function and improvements in those results by using a sidelobe-reduction algorithm. We demonstrated the ability of both a sidelobe-reduction algorithm and a super-resolution algorithm to improve the imagery from a coherent sensor, such as a heterodyne array sensor. We analyzed the trade-off between sparsity of array elements and number of speckle realizations. We designed some experiments for determining missile size and dynamics parameters at the Innovative Science and Technology Experimental facility (ISTEF). We developed an approach for preconditioning the autocorrelation estimates in imaging correlography to obtain improved image reconstruction, and demonstrated it on laboratory data.			
14. SUBJECT TERMS Laser Imaging, Laser Speckle, Target Characterization, Target Tracking, Sparse Arrays, Atmospheric Turbulance, Image Enhancement		15. NUMBER OF PAGES 76	
		16. PRICE CODE	
17. SECURITY CLASSIFICATION OF REPORT UNCLASSIFIED	18. SECURITY CLASSIFICATION OF THIS PAGE UNCLASSIFIED	19. SECURITY CLASSIFICATION OF ABSTRACT UNCLASSIFIED	20. LIMITATION OF ABSTRACT UNCLASSIFIED

PREFACE

The work reported here was performed in the Advanced Information Systems Group, ERIM International [formerly the Environmental Research Institute of Michigan (ERIM)]. The work was sponsored by the Naval Air Warfare Center (NAWC) Contract No. N-62269-91-C-0526, funded from the Innovative Science and Technology Office of the Strategic Defense Initiative Office (SDIO/IST) via the Naval Command & Ocean Surveillance Center/NRaD. The project monitor at NRaD was Dr. Guy Beaghler and at NAWC was Dr. Jim Verdi.

This final report covers work performed from July 1995 to December 1997. The principal investigator was Dr. James R. Fienup. Additional contributors to this work also included David A. Carrara, Dr. Carl C. Aleksoff, Dr. Joseph C. Marron, and Dr. Richard G. Paxman from ERIM, and Dr. Timothy J. Schulz from Michigan Technological University.

TABLE OF CONTENTS

Preface.....	iii
List of Figures	v
List of Tables.....	vi
1 Introduction and Overview	1
2 Target Parameter Estimation	4
3 Target Support Estimation from the Autocorrelation.....	7
4 Array Sparsity and Speckle Realizations.....	15
5 Isoplanatic Considerations.....	22
6 ISTEf Experimental Design	33
7 Tracking Via Speckles.....	45
Appendix A.....	A-1
Appendix B	B-1
Appendix C	C-1

LIST OF FIGURES

1-1. Laser Illumination and Detection for Imaging and Parameter Estimation.....	1
3-1. Triple Intersection Approach to Estimate Object Support.....	8
3-2. Triple Intersection Approach to Estimate Missile Support.....	9
3-3. Block Diagram of Steps to Improve Image Support Estimation.....	11
3-4. Image, Fourier, and Autocorrelation Steps in Estimating Object Support.....	12
3-5. Autocorrelation and Object Support Estimates for Different Numbers of Speckle Realizations	14
4-1. Object Power Spectral Densities	16
4-2. Array Patterns and their OTF's.....	18
4-3. Arrow and Box+2 Array Patterns	19
5-1a. Isoplanatic Angle vs. Path Length at 0.5 μm Wavelength for Various C_n^2	26
5-1b. Isoplanatic Angle vs. Path Length at 1.0 μm Wavelength for Various C_n^2	27
5-1c. Isoplanatic Angle vs. Path Length at 10 μm Wavelength for Various C_n^2	28
5-2a. Isoplanatic Patch Diameter vs. Path Length at 0.5 μm Wavelength for Various C_n^2	29
5-2b. Isoplanatic Patch Diameter vs. Path Length at 1.0 μm Wavelength for Various C_n^2	30
5-2c. Isoplanatic Patch Diameter vs. Path Length at 10 μm Wavelength for Various C_n^2	31
5-3. Critical C_n^2 for an Isoplanatic Patch Diameter of 12 m vs. Path Length for Various Wavelengths.....	32
6-1. The Speckle Based Concept.....	33
6-2. The Baseline Experimental Arrangement	37
6-3. Target Mount Assemblies	40
7-1. Rotation Geometry.....	46

LIST OF TABLES

4.1. Number of Speckle Realizations Required.....	21
6.1. Potential Experiments.....	34
6.2. Lasers.....	35
6.3. Cameras.....	36
6.4. Scud Missile Properties.....	39

1 INTRODUCTION AND OVERVIEW

This report describes an effort to provide signal processing tools and perform experimental design for unconventional imaging and parameter estimation from laser-illuminated targets at long ranges, using arrays of detectors without the need for imaging optics. This allows for an inexpensive, lightweight, rapidly steerable receiver capable of very fine resolution. This approach could result in a system for rapidly gathering information about missiles or aircraft in flight.

As illustrated in Figure 1-1, the approach is to illuminate a distant target with a coherent laser. Instead of forming an image with bulky imaging optics (a telescope), we instead measure the laser light backscattered from the target with an array of light-bucket detectors with no intervening optics. This measurement scheme allows for a much cheaper, lighter-weight receiver than a conventional telescope. The array could either be filled with detectors or could be sparsely populated with detectors, making it even more light-weight and inexpensive. The array could either be a heterodyne sensor (mixing the light from the target with light direct from the laser) or direct detection (measuring only the intensity of the light from the target). In either case, significant computer processing is required to convert the output from the detectors into usable information, whether in the form of an image or in the form of useful target

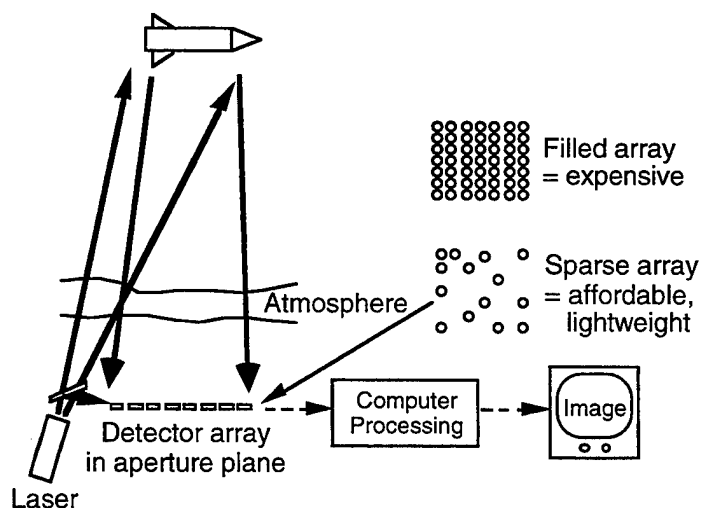


Figure 1-1. Laser Illumination and Detection for Imaging and Parameter Estimation.

parameters, such as shape, length, width, and trajectory.

At the beginning of the program, it was thought that we might receive heterodyne data from another effort, and that we could use it for imaging experiments. As the program developed, it became apparent that heterodyne data would not be available in a timely fashion, so most of our effort was aimed at using direct-detection data. This data, a coherent laser speckle pattern, is equivalent to the intensity of the Fourier transform of the coherently illuminated object. It is useful primarily for target parameter estimation.

Under this effort we accomplished the following.

We demonstrated the utility of a sidelobe-reduction algorithm and a superresolution algorithm to coherent optical imagery, such as heterodyne array imaging. Although the algorithms were developed for synthetic aperture radar imagery, we showed that they also worked well for an optical image that contains fine detail and specular reflections, as would often be found for a laser-illuminated object. It gave less improvement for a bland, diffuse object. This is described in Appendix A.

We catalogued the target parameters that could be characterized by measuring laser speckle parameters. This is described in Section 2.

We developed an approach to achieving improved accuracy in estimating the shape of the object from laser speckle patterns, using the sidelobe-reduction algorithm and an autocorrelation unfolding approach. This is described in Section 3.

We analyzed the signal-to-noise ratio for laser imaging with sparse arrays of detectors, and showed the trade-off between the number of detectors and the degree of array sparsity. This is described in Section 4.

We performed calculations of isoplanatic angles that would impact any experiments at ISTEf, as shown in Section 5.

We developed a plan for experiments to be performed at ISTEf for measuring target shapes and motions from backscattered laser speckle patterns. This is described in Section 6.

Section 7 gives additional detail on tracking via speckles, one of the target parameters discussed in Section 2.

Imaging correlography involves averaging the autocovariance of the pupil-plane laser speckle intensity pattern to arrive at an estimate of the magnitude of the Fourier transform of the object's incoherent reflectivity function, then performing phase retrieval on that data to reconstruct an image. We developed a method for preconditioning autocorrelation estimates for imaging correlography. Low-frequency lags are used to control the smoothness of the reconstructed image. This method was demonstrated on laser speckle data gathered in the laboratory. These results were produced at Michigan Technological University and are presented in Appendix B.

A portion of this effort is described in the presentation and proceedings paper in [1.1], which is included as Appendix A. Reference [1.2] describes some of the results of a previous effort that were presented in a conference during the current effort.

- [1.1] "Application of Superresolution Algorithm to Optical Coherent Imaging," J.R. Fienup, M.R. Kosek, and H.C. Stankwitz, in Proc. SPIE 2827-08 Digital Image Recovery and Synthesis III (August 1996) (invited paper).
- [1.2] "Laser Imaging with Sparse Pupil-Plane Detectors," J.R. Fienup, to the Annual Meeting of the O.S.A., Portland, Oregon, 11-15 September 1995.

References are at the end of each section.

2 TARGET PARAMETER ESTIMATION

If we illuminate a target with a laser and detect the backscattered, speckled intensity pattern, as illustrated in Figure 1.1, what can we tell about the target?

If the measured intensity is $I(x, t)$, where x is a 2-D spatial coordinate and t is time, then a valuable quantity to assess is the correlation function

$$|\mu|^2 = \frac{\langle I(x, t) I(x + \Delta x, t + \Delta t) \rangle}{\langle I(x, t) \rangle^2} - 1 \quad (2.1)$$

where

$$\langle I(x, t) I(x + \Delta x, t + \Delta t) \rangle = \frac{1}{M} \sum_{m=1}^M I(x, t_m) I(x + \Delta x, t_m + \Delta t) \quad (2.2)$$

Speckles with perfect correlation (spatial and temporal) have $|\mu| = 1$. When the speckle decorrelates or "boils," $|\mu| < 1$.

If the target rotates with angular rate Ω , then the peak of $|\mu|$ translates from the origin by a distance Δx_p in the time interval Δt_1 , given by

$$\Omega = \frac{\Delta x_p}{2R\Delta t_1} \quad (2.3)$$

We previously demonstrated this in the laboratory. We can obtain two speckle patterns separated by time Δt_1 either by (a) reading out the speckle pattern quickly, using a fast detector, or (b) double-pulsing the laser, and detect the sum of the two pulses on a CCD camera. A problem with this measurement is that the effective speckle velocity at the detector,

$$v_s = \frac{\Delta x_p}{\Delta t_1} = 2\Omega R, \quad (2.4)$$

can also be caused by a transverse translation of the target with a velocity $v_s/2$. The total speckle velocity is given by

$$v_s = 2\Omega R + 2v_{\text{target}} \quad (2.5)$$

Take the case where a target is at a range of $R = 100$ km and $\Omega = 0.2$ radians/sec. Then $2\Omega R = 40,000$ m/sec, which is much faster than any missile. Hence if the target is rotating, then its rotation rate can easily dominate its velocity in its effect on the velocity of the speckles. By observing the speckle from the target over time, it might be possible to determine its rough trajectory and its velocity and separate the effects of its rotation rate. Since the speckle velocity is so sensitive to the rotation rate, this affords a potentially very sensitive method of determining the rotation rate of the target. Section 7 gives additional details on measuring rotation rates.

The half-width of $|\mu|$ is related to the width, d_o , of the object through the relationship

$$\Delta x_{\text{width}} = \frac{\lambda R}{d_o} . \quad (2.6)$$

Hence we can determine the length and width (projected onto a plane perpendicular to the line of sight) of the target. As described in Section 3, we can also determine more details about the shape of the object.

If the object consists of two parts (for example, a bus and an ejected warhead), with separation S between them, then $|\mu|$ will have a main lobe and a side lobe, with the separation between them being $\lambda R/S$. Hence we can measure the distances between separated parts of the object (projected onto a plane perpendicular to the line of sight).

If the object is changing, say due to thermal effects, then the speckle pattern will decorrelate with time, when the object is stationary. Hence the decay of $|\mu(t)|$ with time is a measure of changes in the object.

If we measure at multiple wavelengths, then the decorrelation of $|\mu|$ with wavelength gives a measure of the depth of the object (along the line of sight).

Several other discriminants that could be considered include the following. The color, or spectral reflectivity, of the object can be used to determine its surface materials. Polarized light can be used to determine something about the surface texture

of the object (rough or smooth), and whether there is significant 3-D geometry effects (multiple bounces before the light returns).

3 TARGET SUPPORT ESTIMATION FROM THE AUTOCORRELATION

By the “support” of the object we mean the set of points over which it may be nonzero, or its shape or outline. We can determine bounds on the support of the object from the direct-detected laser speckle pattern, even if the atmospheric turbulence causes a phase error in the optical fields that would blur the image gathered by a telescope. This will allow us to determine the length, width, and orientation of the object, which will be useful in classification and trajectory estimation. This section describes advanced methods we developed for support estimating from laser speckle patterns.

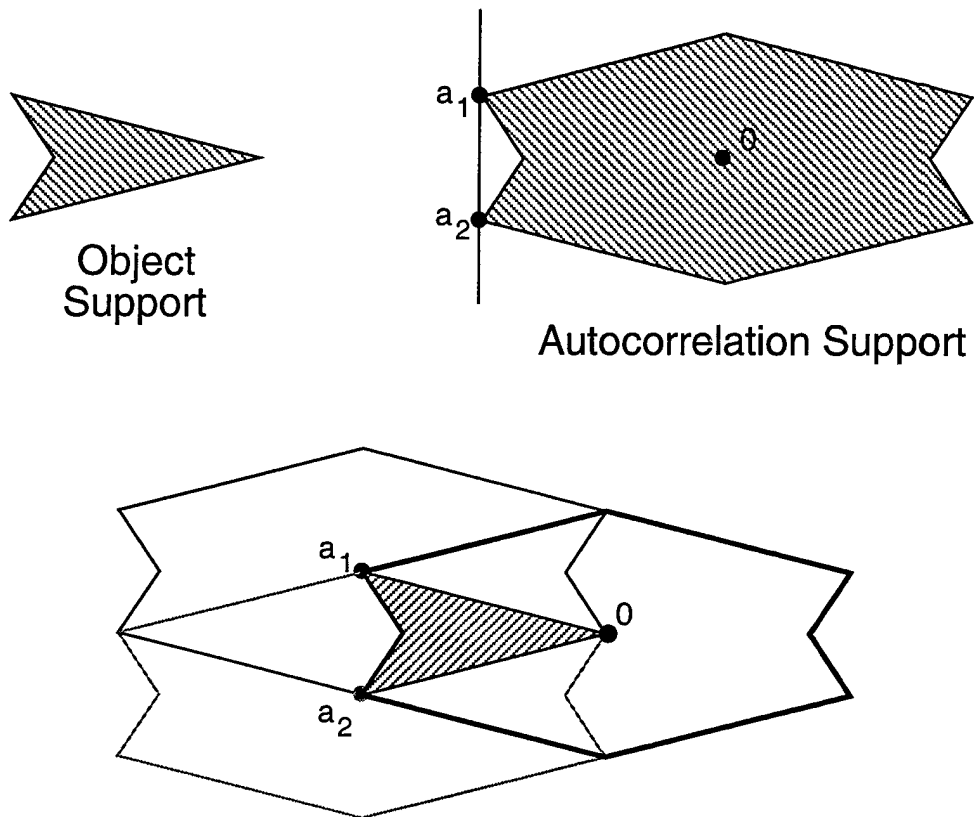
Suppose that the ideal optical field at the detector array is $F_k(u)$, and the corresponding diffraction-limited image is $f_k(x)$, where k is the number of the speckle realization and u and x are 2-D spatial coordinates. If we could make heterodyne measurements of the optical fields, we would have $G_{dk}(u) = F_k(u) \exp[i\phi(u)]$, where $\phi(u)$ are the phase errors. By inverse Fourier transforming we would arrive at a blurred image $g_{dk}(x)$. If instead we measure the intensity pattern $|G_{dk}(u)|^2$, we can inverse Fourier transform to arrive at the autocorrelation function

$$r_k(x) = \mathcal{F}^{-1}[|G_{dk}(u)|^2] = \sum_{x'} g_{dk}(x') g_{dk}^*(x' - x) = \sum_{x'} f_k(x') f_k^*(x' - x) . \quad (3.1)$$

Note that the autocorrelation of the blurred image, $g_{dk}(x)$, is equal to the autocorrelation of the ideal image, $f_k(x)$, and it can be computed from the direct-detected speckle intensity without the need for heterodyne detection. By averaging over many speckle realizations, we can arrive at a speckle-averaged autocorrelation,

$$r_I(x) = K^{-1} \sum_k |r_k(x)|^2 . \quad (3.2)$$

From this autocorrelation we can estimate the shape of the object using techniques described in Reference 3.1. Figure 3-1 illustrates this approach.

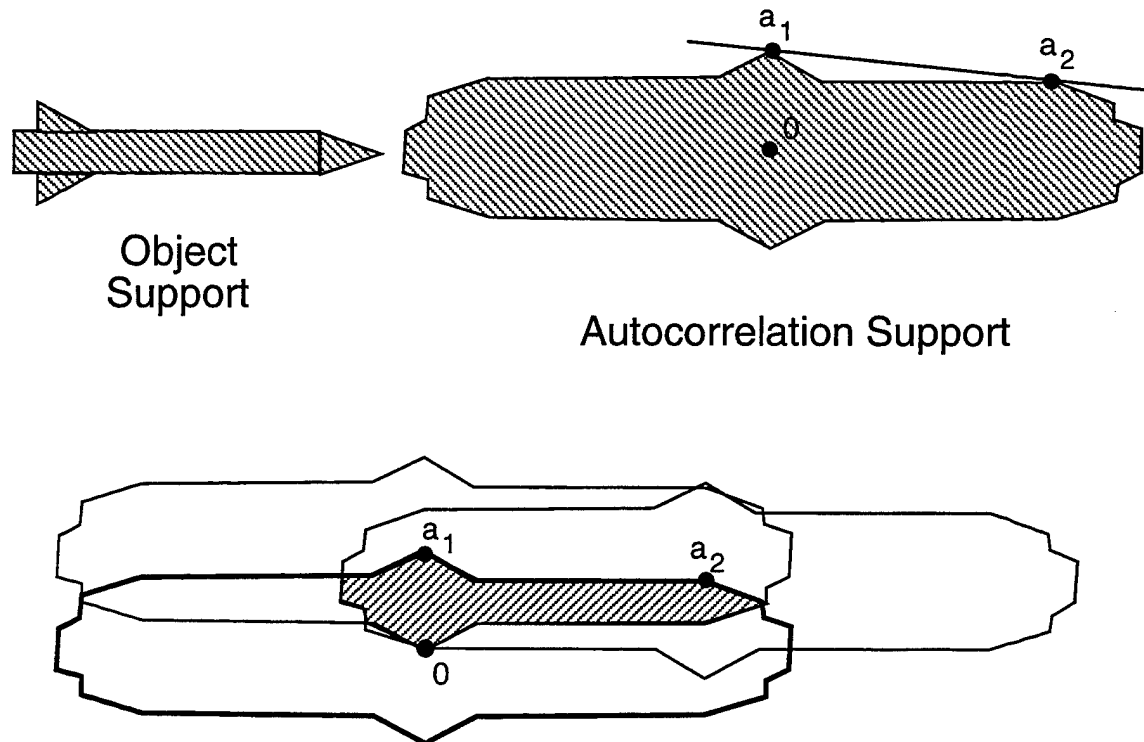


Triple Intersection of Autocorrelation Supports

Figure 3-1. Triple Intersection Approach to Estimate Object Support. If a line can be drawn tangent to the support of the autocorrelation so that it intersects it at exactly two points (a_1 and a_2), then the intersection of three translates of the autocorrelation support (centered at the origin, at a_1 , and at a_2) define a “locator set” that must contain any object that could have given rise to the autocorrelation support [3.1]. In this case, the locator set is exactly the support of the original object. More often the locator set is larger than the true object and gives an upper bound on the support of the object.

We performed support-estimation experiments with images of missiles, which are germane to the mission of SDIO. Figure 3-2 shows a triple intersection result assuming we had available the exact autocorrelation support for a missile. In this case the triple intersection tightly bounds the shape of the missile, giving us good information about the length, width, and shape of the missile. However, such idealized autocorrelation information is not available. The problem is that autocorrelations computed from laser-illuminated objects suffer from both diffraction and speckle. Diffraction causes sidelobes that are energy outside the true support of the autocorrelation, making the

autocorrelation appear larger than it really is. Speckle causes energy drop-outs within the support of the autocorrelation, making parts of it to disappear.



Triple Intersection of Autocorrelation Supports

Figure 3-2. Triple Intersection Approach to Estimate Missile Support.

We attacked the problems of speckle drop-out and diffraction to get better estimates of the autocorrelation support, which would allow us to get better estimates of the shape of the object. Figure 3-3 shows a block diagram of the steps we investigated for accomplishing this. Figure 3-4 shows an example of each step for a simulated image of a missile. The parts (a, b, etc.) of Figure 3-4 are labeled in the diagram in Figure 3-3 and are referred to in the discussion below.

We started with a CAD/CAM model of a missile and computed a rendering of it (a). From that we computed speckle realizations and Fourier transformed them to get the coherent optical fields at the detector, $F_k(u)$. The detector measures only the intensity,

$|F_k(u)|^2$ (b). We want to compute the Fourier transform of this to arrive at the autocorrelation function. However, we first subtract the mean intensity to get rid of a delta-function term that would otherwise appear superimposed on the autocorrelation function [3.2]. To estimate this mean, we average the intensity over the area of the detector (u) or, in 2-D (u, v), and over the speckle realizations. We then inverse Fourier transform the result to arrive at a speckled autocorrelation function (c). To reduce the sidelobes of the autocorrelation function, we apply the Spatially Variant Apodization (SVA) algorithm (d) [3.3]. Then we average the intensities of the speckled autocorrelations over all the available speckle realizations to arrive at a speckle-reduced autocorrelation (e, shown for averaging 5 realizations). In the example, note that some small residual sidelobes are present, emanating from the origin. This is due to an imperfect estimate of the bias that was subtracted. We threshold this result (e) to arrive at an estimate of the support of the autocorrelation function (f). We presently pick the threshold by trial and error. Further research would be needed to pick the threshold value automatically. We fill in the speckle nulls in this autocorrelation support by a “closing” operation from image algebra (a dilation followed by an erosion), to get our final autocorrelation support estimate (g). We then use the triple intersection rule described above to get an upper bound on the object support (h). We use this upper bound as an estimate of the object support. As suggested in Figure 3-4 (i), we can use this to estimate the length, width, and angle of the target. This information should be useful for missile typing (classification) and determination of missile trajectory. Recall that this information arises from the pupil-plane intensity patterns, as shown in Figure 3-4(b), which looks nothing like an image and does not require optics to form an image.

Multiple aperture plane
speckle realizations

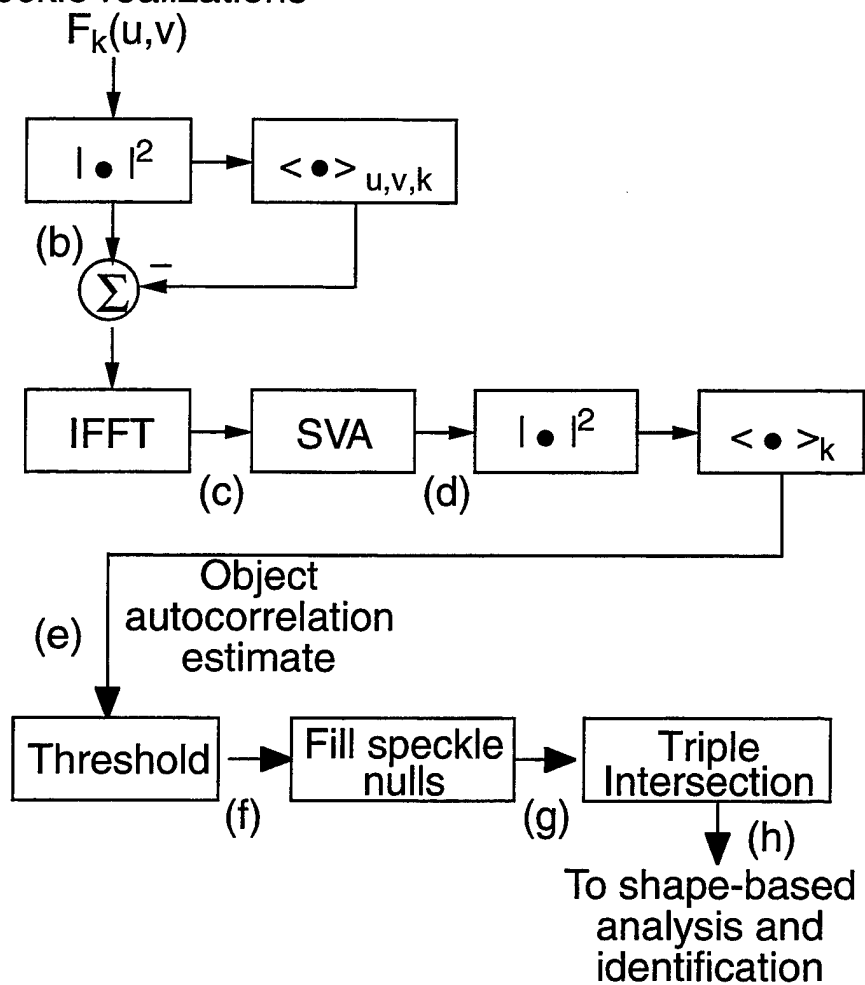
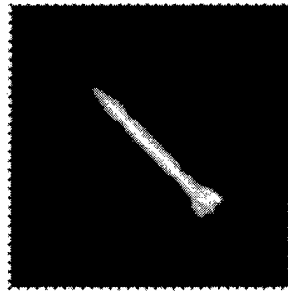
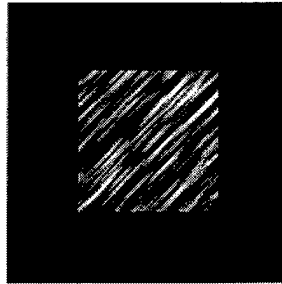


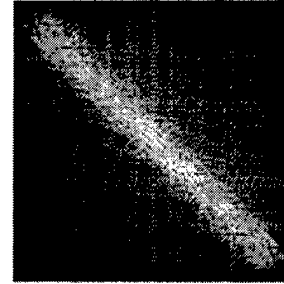
Figure 3-3. Block Diagram of Steps to Improve Image Support Estimation.



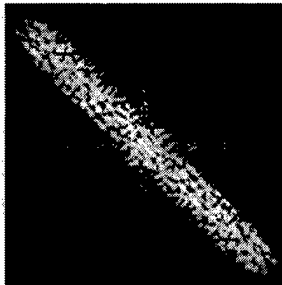
(a) Incoherent Image



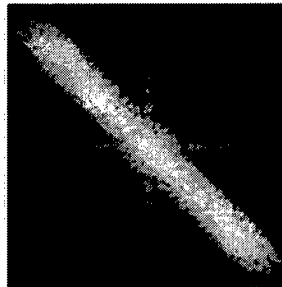
(b) Aperture Plane Intensity



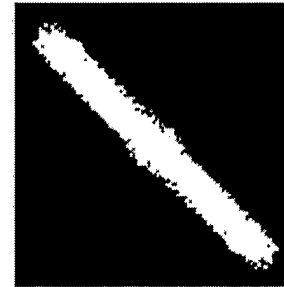
(c) Coherent AutoCorrelation



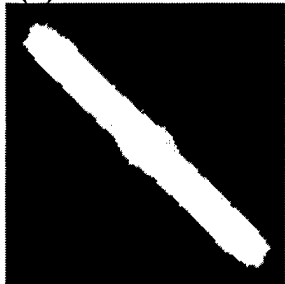
(d) AC after SVA



(e) Average AC



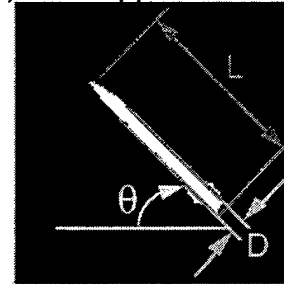
(f) AC Support Estimate



(g) Filled AC Support



(h) Object Support Bound



(i) Potential Processing Result

Figure 3-4. Image, Fourier, and Autocorrelation Steps in Estimating Object Support.

Figure 3-5 shows the results of averaging different numbers of speckle frames, from $K = 1$ frame (no averaging), to $K = \infty$, which is equivalent to an incoherent autocorrelation. The object support estimate improves as we increase the number of speckle frames averaged.

With these results we have shown that, with advanced signal processing methods, we can obtain reasonable estimates of the length, width, and orientation of a missile from the intensity of laser light backscattered from it, without using imaging optics. These simulations assumed that the laser power was high enough that speckle noise statistics dominates over photon noise. Further research would be necessary to determine the effect of photon noise on the result.

References

- 3.1 T.R. Crimmins, J.R. Fienup and B.J. Thelen, "Improved Bounds on Object Support from Autocorrelation Support and Application to Phase Retrieval," J. Opt. Soc. Am. A 7, 3-13 (1990).
- 3.2 P.S. Idell, J.R. Fienup and R.S. Goodman, "Image Synthesis from Nonimaged Laser Speckle Patterns," Opt. Lett. 12, 858-860 (1987).
- 3.3 H.C. Stankwitz, R.J. Dallaire, and J.R. Fienup, "Non-linear Apodization for Sidelobe Control in SAR Imagery," IEEE Trans. AES 31, 267-278 (1995).

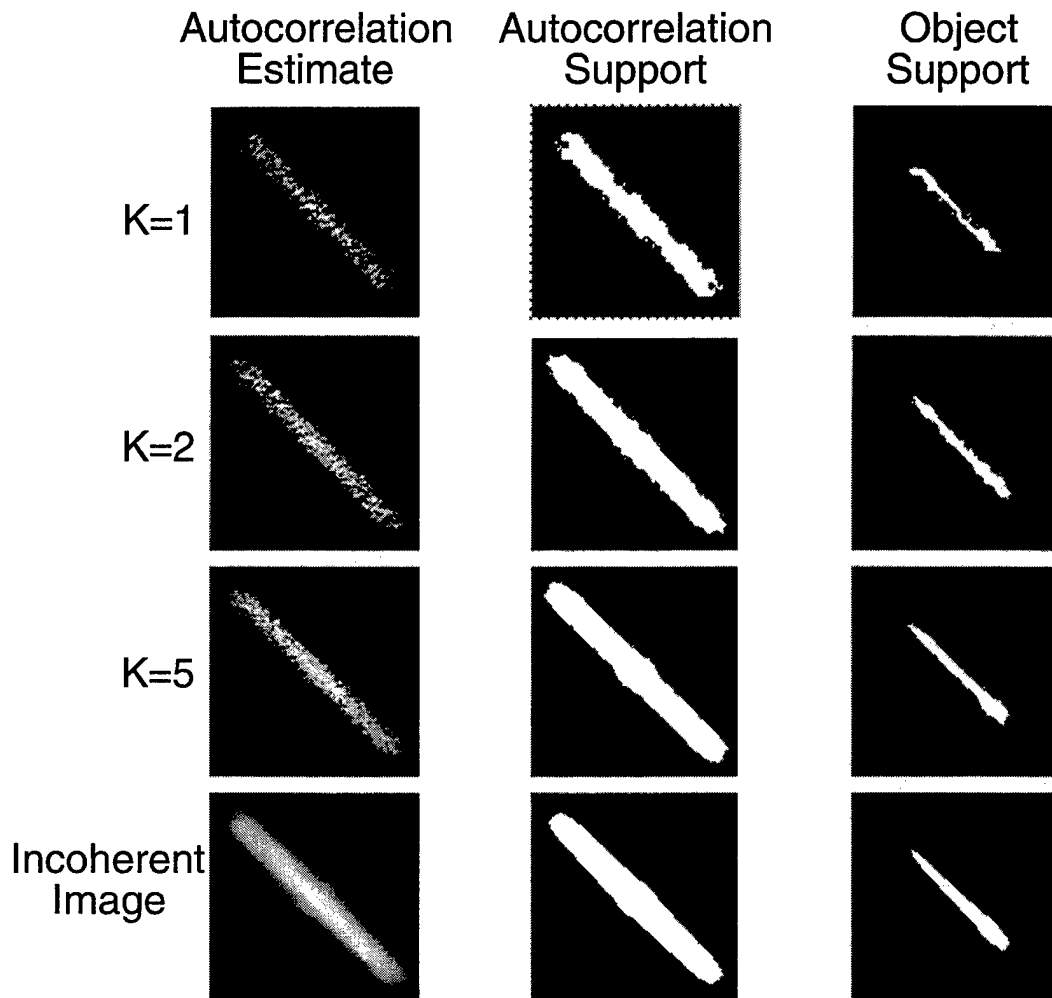


Figure 3-5. Autocorrelation and Object Support Estimates for Different Numbers of Speckle Realizations.

4 ARRAY SPARSITY AND SPECKLE REALIZATIONS

The signal-to-noise ratio (SNR) of our autocorrelation estimates computed from the pupil-plane intensity measurements from a laser-illuminated object depends on the light level, the size of the detector array, the sparsity of the array (the array fill factor), and the number of speckle realizations over which we average. Suppose that we pick an array diameter to achieve the desired resolution on the target ($\rho = \lambda R/D$, where ρ is resolution, λ wavelength, R range, and D diameter of the detector array). We can make the array cheaper and more light weight by sparsely populating it with detector elements, but then we require a greater number of speckle realizations (i.e., a greater collection time) to achieve the required SNR.

For heterodyne array imaging, the SNR at a given spatial frequency (u, v) is given by [4.1]

$$\text{SNR}(u, v) \approx \sqrt{K n_s \text{OTF}(u, v)} |\mu(u, v)|, \quad (4.1)$$

and for correlography (measuring speckle intensities in the pupil plane) [4.2],

$$\text{SNR}(u, v) \approx \sqrt{(K/3) n_s \text{OTF}(u, v)} |\mu(u, v)|^2, \quad (4.2)$$

where

K = number of speckle realizations

n_s = number of independent pupil-plane detectors

$n_s \text{OTF}(u, v)$ = number of redundant measurements at (u, v)

$|\mu(u, v)|^2$ = normalized power spectral density of object intensity

The approximations above are good when speckle noise dominates (for more than two detected photons per speckle) and for the mid- to upper spatial frequencies where $|\mu(u, v)|^2$ is small.

We see that, for either modality, the SNR goes as the square root of $n_s \text{OTF}(u, v)$, which in turn depends on the number of detectors in the array, the sparsity of the array, and the particular configuration (geometrical arrangement) of the elements of

the array. A decrease in $n_s \text{OTF}(u, v)$ by some factor can be made up for by a proportional increase in K .

The power spectral density, $|\mu(u, v)|^2$, of the object depends greatly on the type of object, as illustrated in Figure 4-1. For point-like objects (e.g., stars) it falls off slowly with spatial frequencies. As the object becomes more extended, $|\mu(u, v)|^2$ drops off more rapidly with spatial frequency. A rule of thumb (by F. Roddier) is that if, at a given maximum spatial frequency u_r we can resolve n_{bp} bright points, then $|\mu(u_r)|^2 \approx 1/n_{bp}(u_r)$. Hence the performance depends on the spatial frequency content, or the structure, of the object, as well as on the amount of signal collected.

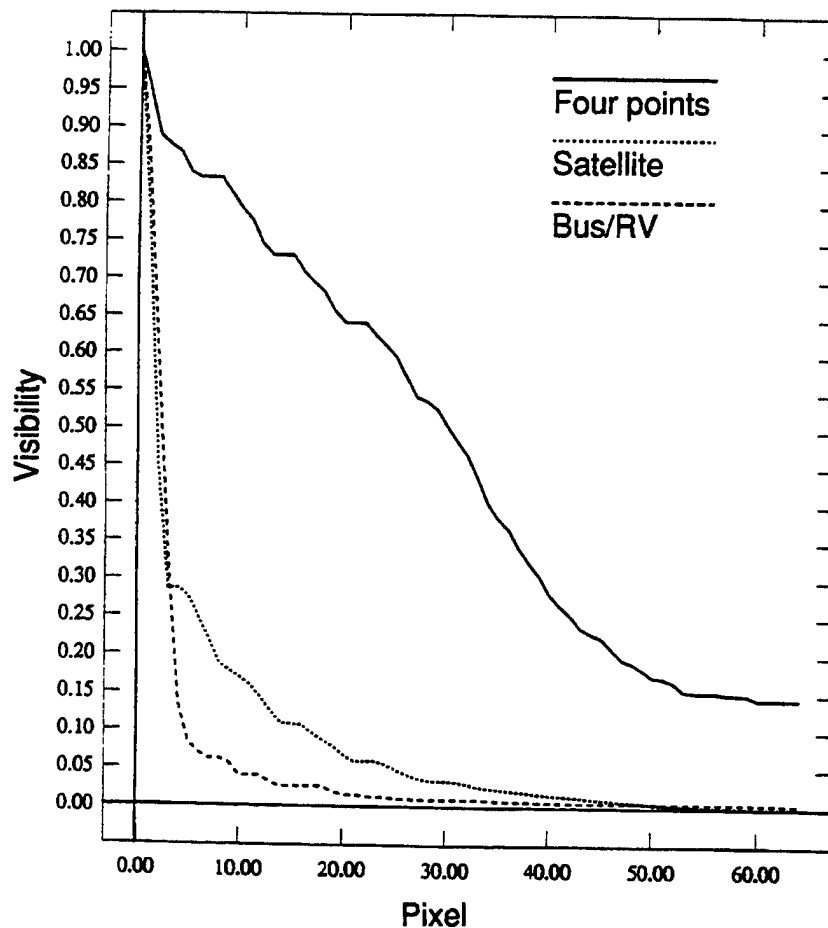
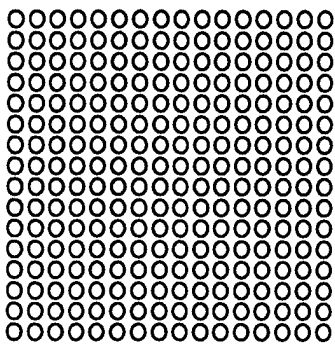


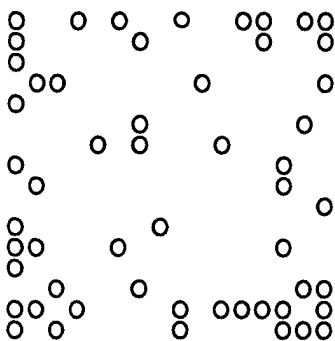
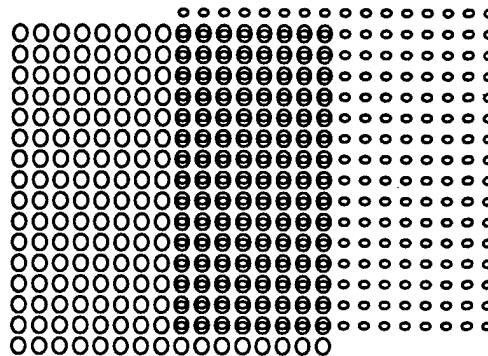
Figure 4-1. Object Power Spectral Densities

We find that, since $|\mu(u, v)|^2$ falls off for the highest spatial frequencies as does $\text{OTF}(u, v)$, we can rarely have good SNR at the highest spatial frequencies. We are better off comparing performance at the middle spatial frequencies. Hence we concentrate on the spatial frequency $u = (1/2) u_{\max}$.

Now consider the term $n_s \text{OTF}(u, v)$, the number of redundant measurements. As illustrated in the top half of Figure 4-2, the OTF, which is given by the autocorrelation of the aperture function, normalized to be unity at the origin, is about 0.5 for a filled aperture at $u = (1/2)u_{\max}$. That is, when the aperture is sheared by half its width, about half of the sheared elements fall on the positions of the original elements, and $\text{OTF}(u_{\max}/2) = 1/2$. For a nonredundant aperture (not shown, since none are known to exist for the 2-D aperture sizes shown), there would be only a single overlapping element, and so the OTF would be $1/N$, where N is the number of nonzero elements and N/M^2 is the aperture fill ratio. So nonredundant apertures have very low values of $n_s \text{OTF}(u, v)$ and require M^2/N times more speckle realizations than a filled aperture of the same diameter. The bottom example in Figure 4-1 shows an aperture with $N = 54$ subapertures designed by P. Henshaw [4.3] to be minimally redundant. Depending on the spatial frequency, it has $n_s \text{OTF}(u, v) =$ anywhere between one and several overlaps, and has 6 for the spatial frequency shown, where $\text{OTF}(u, v) = 6/54 \approx 0.11$. Figure 4-3 shows the arrow and box+2 array patterns, which we invented. The former has $n_s \text{OTF} \geq 1$ and the latter has $n_s \text{OTF} \geq 2$ for all spatial frequencies, using a relatively small number of array elements, and both arrays are easily scalable to any size desired.



Filled Aperture -- 256 subapertures



Genetic Algorithm -- 54 subapertures

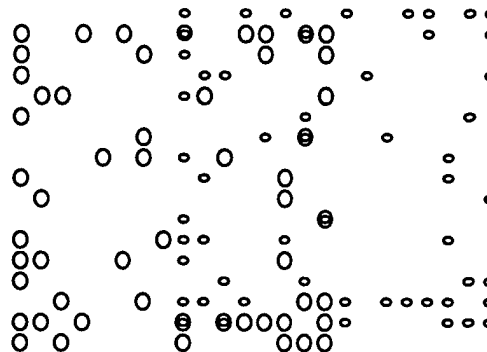
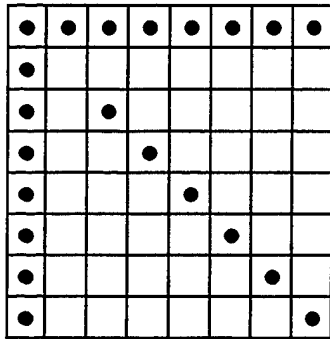
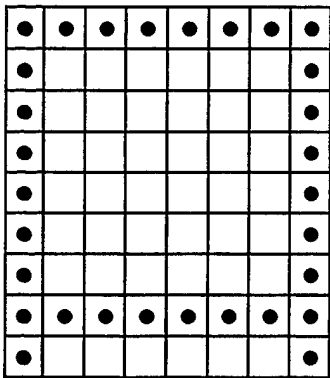


Figure 4-2. Array Patterns and their OTF's. Top: filled aperture; bottom: pattern generated by genetic algorithm



“Arrow” Array
 $3M - 3$ subapertures
 to cover same area
 as $M \times M$ filled array
 with no Fourier gaps



“Box + 2” Array
 $4M - 2$ subapertures
 to cover same area
 as $M \times M$ filled array
 with minimum of
double redundancy

Figure 4-3. Arrow and Box+2 Array Patterns.

Now let's compare a sparse array with N elements to a filled array with $M \times M = M^2$ elements. Both cover a $(2M - 1) \times (2M - 1)$ array in Fourier (OTF) space. Including the redundancy factor for each spatial frequency, with N elements we measure $2N(N - 1)$ frequencies (not counting d.c.). An ideal (fictitious) nonredundant array covering $(2M - 1) \times (2M - 1)$ Fourier samples would require N elements, where $2N(N - 1) = (2M - 1)^2 - 1$, or $N \approx \sqrt{2} M$ for large M . A realizable minimally redundant array, the arrow array, requires $N = 3M - 3$ elements. The cost savings in array elements, compared with the filled aperture, is a factor of $M^2/(3M - 3) \approx M/3$, which can be a large number. But at $u = (1/2)u_{\max}$, the filled aperture has $n_s \text{OTF} = M^2/2$, versus 1 for the weakest spatial frequency of the minimally redundant array. Hence the factor of $M/3$ in cost savings must be weighed against the factor of $M^2/2$ in integration time to get that factor times as many speckle realizations.

The number of speckle realizations that are available limits how great an increase in SNR is possible. To get a new speckle realization, the target must rotate through an angle $D/(2R) = \lambda/(2\rho)$, where

D = aperture diameter,

R = range to target,

λ = wavelength, and

ρ = resolution.

However, if an object rotates too much, it no longer looks like the same objects. We use a rule of thumb that the object can rotate by ρ/d_o radians before it changes significantly, where d_o is the diameter of the object. This allows for $(\rho/d_o)(2\rho/\lambda) = 2\rho/(d_o\lambda)$ speckle realizations. For example, if the object diameter is $d_o = 5$ m, $\rho = 0.20$ m, and $\lambda = 1$ μ m, then we can have up to 16,000 speckle realizations, if the laser and detector are fast enough to detect in the time that it takes the speckle pattern to move by D .

To achieve a given SNR, we find that for heterodyne array imaging the number of speckle realizations we need is

$$K = \frac{\text{SNR}^2}{n_s \text{OTF } |\mu|^2} \quad (4.3)$$

and for correlography is

$$K = \frac{3 \text{SNR}^2}{n_s \text{OTF } |\mu|^4} . \quad (4.4)$$

If we assume that we need a $\text{SNR} = 3$ at the spatial frequency $u = (1/2) u_{\text{max}}$, then Table 4.1 compares the number of speckle realizations for (a) filled versus nonredundant (or minimally redundant) arrays, (b) for heterodyne imaging and correlography, (c) for three different object types, and (d) for array sizes 8×8 , 32×32 , and 128×128 . From this we see that nonredundant and minimally redundant arrays are generally suitable (require less than 10^5 speckle realizations) for coherent illumination only for point-like object or small extended objects. For large, extended objects, nonredundant arrays are not suitable, and one needs arrays with large amounts of redundancy (such as a filled array).

Table 4.1. Number of Speckle Realizations Required:

object type:		two glints	small extended	large extended
MxM	Modality	$ \mu = 0.5$	$ \mu = 0.1$	$ \mu = 0.01$
		filled \leftrightarrow nonred.	filled \leftrightarrow nonred.	filled \leftrightarrow nonred.
8x8	heterodyne	1 \leftrightarrow 36	28 \leftrightarrow 900	n/a
8x8	correlography	14 \leftrightarrow 432	8,438 \leftrightarrow 2.7×10^5	n/a
32x32	heterodyne	1 \leftrightarrow 36	2 \leftrightarrow 900	176 \leftrightarrow 90,000
32x32	correlography	1 \leftrightarrow 432	527 \leftrightarrow 2.7×10^5	$5.3 \times 10^6 \leftrightarrow 2.7 \times 10^9$
128x128	heterodyne	1 \leftrightarrow 36	1 \leftrightarrow 900	11 \leftrightarrow 90,000
128x128	correlography	1 \leftrightarrow 432	33 \leftrightarrow 2.7×10^5	$3.3 \times 10^5 \leftrightarrow 2.7 \times 10^9$

References

- 4.1 P.S. Idell and A. Webster, "Resolution Limits for Coherent Optical Imaging: Signal-to-Noise Analysis in the Spatial-Frequency Domain," J. Opt. Soc. Am. A **9**, 43-56 (1992).
- 4.2 K. O'Donnell, "Time-Varying Speckle Phenomena in Astronomical Imaging and in Laser Scattering," Ph.D. Thesis, University of Rochester, Rochester, NY (1983).
- 4.2 P.D. Henshaw and N.R. Guivens, Jr., "Genetic Algorithms for Unconventional Imaging," in *Inverse Optics III*, Proc. SPIE **2241**, 257-265 (April 1994).

5 ISOPLANATIC CONSIDERATIONS

Introduction

We are interested in determining what types of information can be obtained with a detector array acquisition system that captures a speckle pattern formed from a missile illuminated with coherent laser light. Under consideration is using the speckle for imaging, target shape discrimination (missile typing) via speckle shapes, and target rotation rate determination via speckle motion. Atmospheric turbulence can affect the detected speckle pattern and hence the quality of the target measurements. The most stringent requirements on the atmospheric turbulence for the various techniques is for generating an image. It requires that the received wavefront from each scatterer on the target propagate through nearly the same atmospheric distribution. This is known as the isoplanatic requirement. Our goal here is to calculate some of the limitations for missile imaging via speckle as given by isoplanatic relationships.

Atmospheric turbulence causes spatially and temporally random fluctuations in the index of refraction of the atmosphere, which then results in random spatial and temporal variations in the phase of an propagating optical wavefront. Although the fundamentally local change is phase, further (far field) propagation of the phase aberrated wave can also lead to amplitude variations in the wavefront. In our considerations here, we are assuming that only phase variations in the wavefronts are significant and the wavefronts are uniform in amplitude for both the target illumination wavefront and in the scattered wavefront.

We also need to distinguish between short exposure recordings of the speckle pattern and long exposure recordings. By short exposure recording we mean that the atmosphere can be assumed to be frozen in its configuration during the exposure. Typically, this is true for exposures < 10 ms. Long exposure recordings must take into account the temporal changes in the atmosphere. Operationally speaking, we are considering the case where the target is illuminated with a long train of short light pulses. For example, we are considering using the ISTEFL Long Pulse Laser that emits a continuous series of $0.6 \mu\text{sec}$ pulses

at a pulse rate of 3 per second. A recording of the speckle pattern for any one pulse would correspond to a short exposure, while long exposure recording is obtained with integration over two or more pulses.

Isoplanatic Expressions and Calculations

For speckle imaging we require that the targets angular extent not exceed the isoplanatic angle θ_0 . Hence, we have the relationship

$$L \leq R \cdot \theta_0 \quad (5.1)$$

where, L is the target's largest dimension and R is the range to the target. The short exposure and long exposure cases have different isoplanatic angles.

The formula for calculating θ_0 is given by [5.1-5.2]

$$\theta_0 = \left[2.91 \cdot \left(\frac{2\pi}{\lambda} \right)^2 \int_0^R d\xi \cdot C_n^2 \cdot \xi^{\frac{5}{3}} \right]^{-\frac{3}{5}} \quad (5.2)$$

where C_n^2 is the structure parameter of the atmospheric index of refraction fluctuations. It is typically a function of altitude and climatic conditions, and is constant in the horizontal direction over uniform terrain. At ground level we can expect values of 10^{-12} to 10^{-14} and at an altitude of 10 km values of 10^{-17} to 10^{-18} for C_n^2 .

For constant C_n^2 (i.e., typically for horizontal propagation) Eq. 2 gives

$$\theta_0 = 0.105 \cdot \left[C_n^2 \cdot \frac{R^{\frac{8}{3}}}{\lambda^2} \right]^{-\frac{3}{5}} = 0.105 \cdot C_n^{\frac{6}{5}} \cdot R^{\frac{8}{5}} \cdot \lambda^{\frac{6}{5}} \quad (5.3)$$

The overall effect on the system response can often best be calculated through the optical transfer function (OTF). The atmospheric OTF contains the factor

$$MTF_{\theta_0} = \exp \left[- \left(\frac{\theta}{\theta_0} \right)^{\frac{5}{3}} \right] \quad (5.4)$$

Hence, at the isoplanatic angle the OTF is reduced by e and the speckle size is correspondingly increased.

Also of interest is what we will call the isoplanatic patch diameter $P_0 = R\theta_0$, which can be written for constant C_n^2 as

$$P_0 = 0.105 \cdot \left[C_n^2 \cdot \frac{R}{\lambda^2} \right]^{-\frac{3}{5}} \quad (5.5)$$

A key point to see is that the isoplanatic patch diameter decreases with increasing range. Hence, there is a maximum range for a desired patch diameter.

The C_n^2 constant varies with altitude and climatic conditions. At ground level we can expect values of 10^{-12} to 10^{-14} and at an altitude of 10 km values of 10^{-17} to 10^{-18} . Figures 1a-1c show plots of the isoplanatic angle versus range for different constant C_n^2 and different wavelengths. Figure 5-2a-5-2c show the corresponding isoplanatic patch diameter as a function of range. It can be seen that at ground level the isoplanatic length can be quite limiting. Working at longer wavelengths and smaller C_n^2 (higher altitudes) alleviates the problem. Figure 5-3 shows the critical values of C_n^2 and range R using equation 5.5 when P_0 is set to 12 meters. The 12 meters is appropriate for the length of scud missiles. Note that if we were to work at a range of 100 km at a wavelength of $0.5 \mu\text{m}$ it is seen that an isoplanatic patch size of 12 m requires a C_n^2 of about 10^{-21} , which typically corresponds to an altitude of over 25 km. This altitude is quite high and, for example, exceeds the 13 km ceiling of the AWACS.

We also know from guide star work that the isoplanatic angle can be a few arcseconds for zenith viewing at a wavelength of $0.5 \mu\text{m}$. This constant, range independent isoplanatic angle, is due to the stars being outside the atmosphere and the calculations are for looking through the entire thickness of the atmosphere. Note that 5 arcseconds equals about $24 \mu\text{rad}$. This isoplanatic angle corresponds to a range of 500 km for a 12 m patch size. Thus, the target must be over 500 km away to be entirely within the isoplanatic angle for zenith viewing. This height exceeds the operating altitude of any tactical missile and hence the technique is not useful for up-looking systems.

As a point of interest, we note that the form of the expression for the atmospheric coherence length r_0 (Fried's coherence radius [5.1,5.2]) is very similar to Eq. 5.2 and that we can write $r_0 = 1.76 \cdot P_0$ for parallel plane illumination and a constant C_n^2 . Thus, within a factor of two, r_0 must be about the same size as the maximum target size.

References

- [5.1]. Beland, R. R., "Propagation through Atmospheric Optical Turbulence," Chapter 2 in Vol. 2 entitled Atmospheric Propagation of Radiation, of The Infrared & Electro-Optical Systems Handbook series.
- [5.2]. Roggemann, M. C. and B. Welsh, Imaging Through Turbulence, CRC Press, New York, 1996.

Isoplanatic Angle θ_0 (radians)

$\lambda = 5 \cdot 10^{-7}$ meters

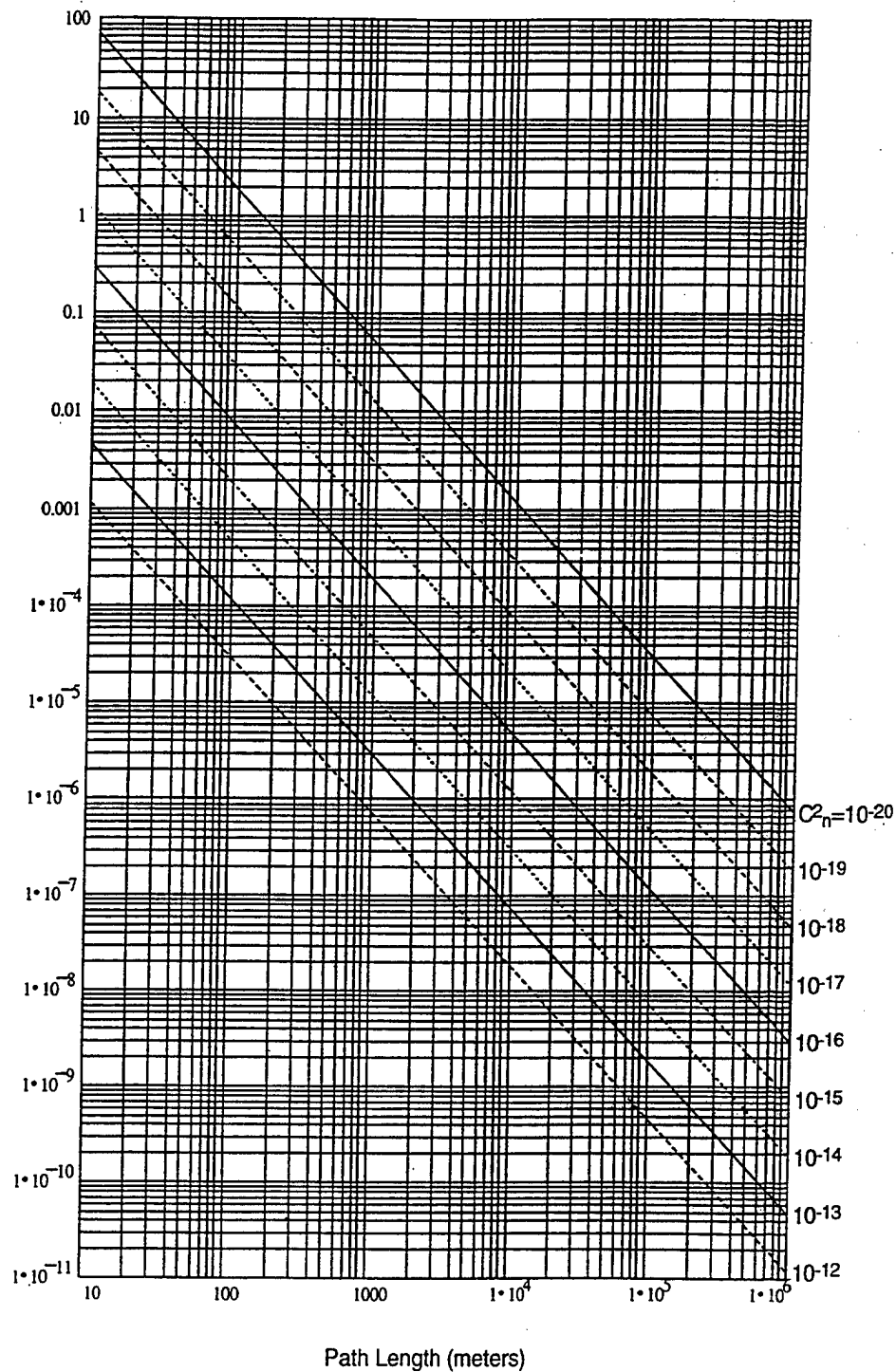


Figure 5-1a. Isoplanatic Angle vs. Path Length at 0.5 μm Wavelength for Various C_n^2

Isoplanatic Angle θ_0 (radians)

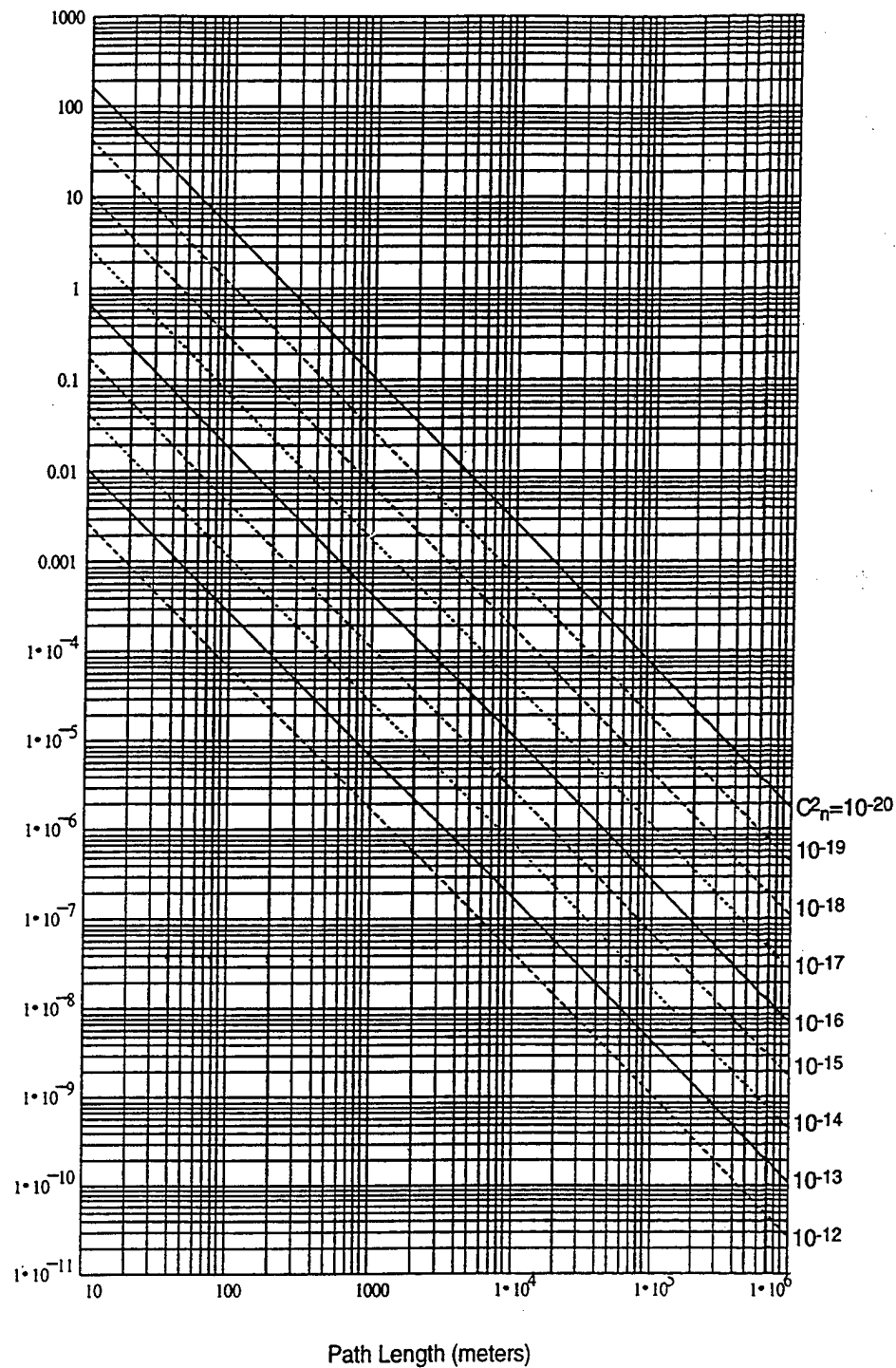
 $\lambda = 1 \cdot 10^{-6}$ meters


Figure 5-1b. Isoplanatic Angle vs. Path Length at 1.0 μm Wavelength for Various C_n^2 .

Isoplanatic Angle θ_0 (radians) $\lambda = 1 \cdot 10^{-5}$ meters

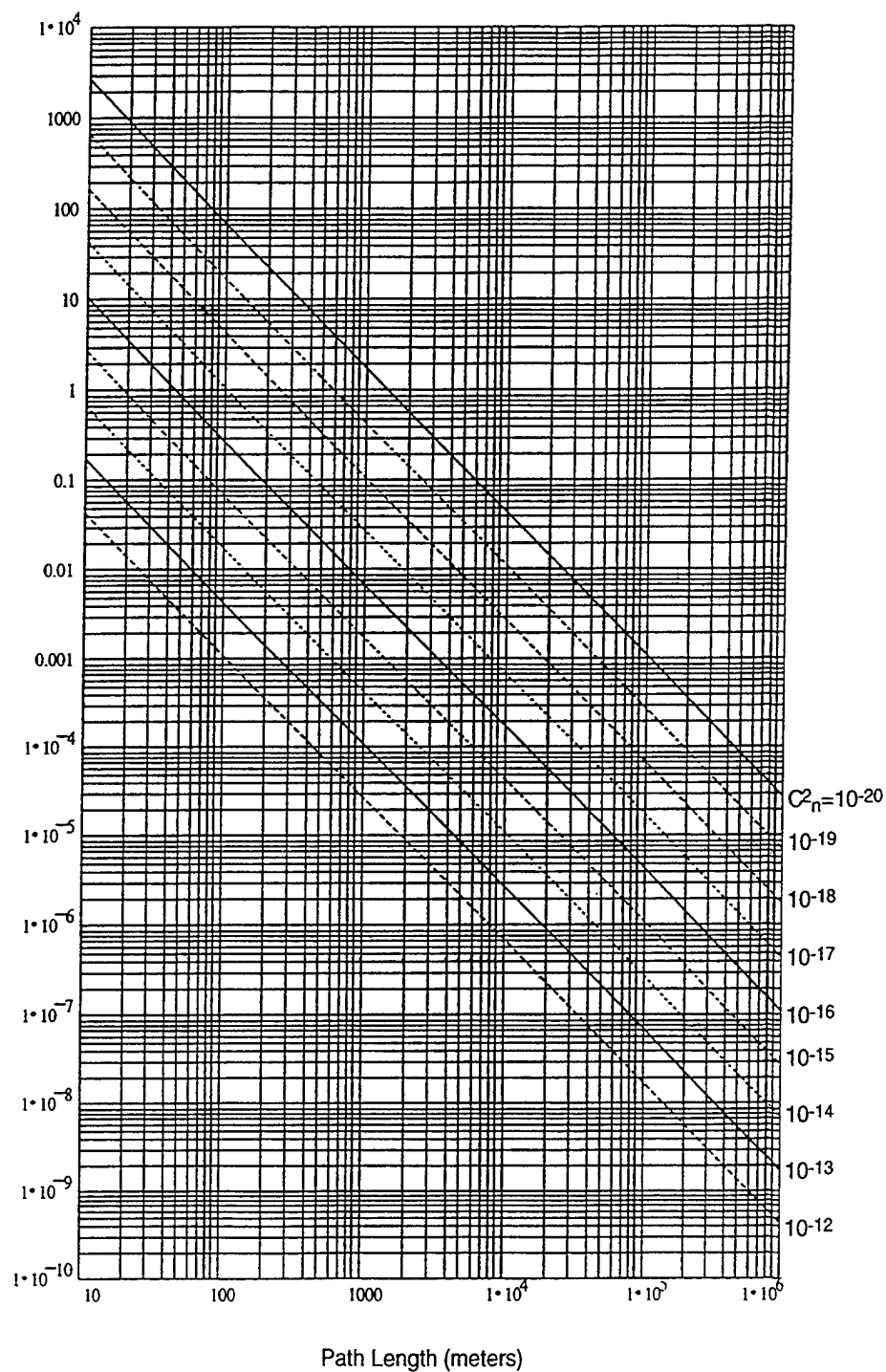


Figure 5-1c. Isoplanatic Angle vs. Path Length at 10 μm Wavelength for Various C_n^2 .

Isoplanatic Patch Diameter p_0 (meters)

$\lambda = 5 \cdot 10^{-7}$ meters

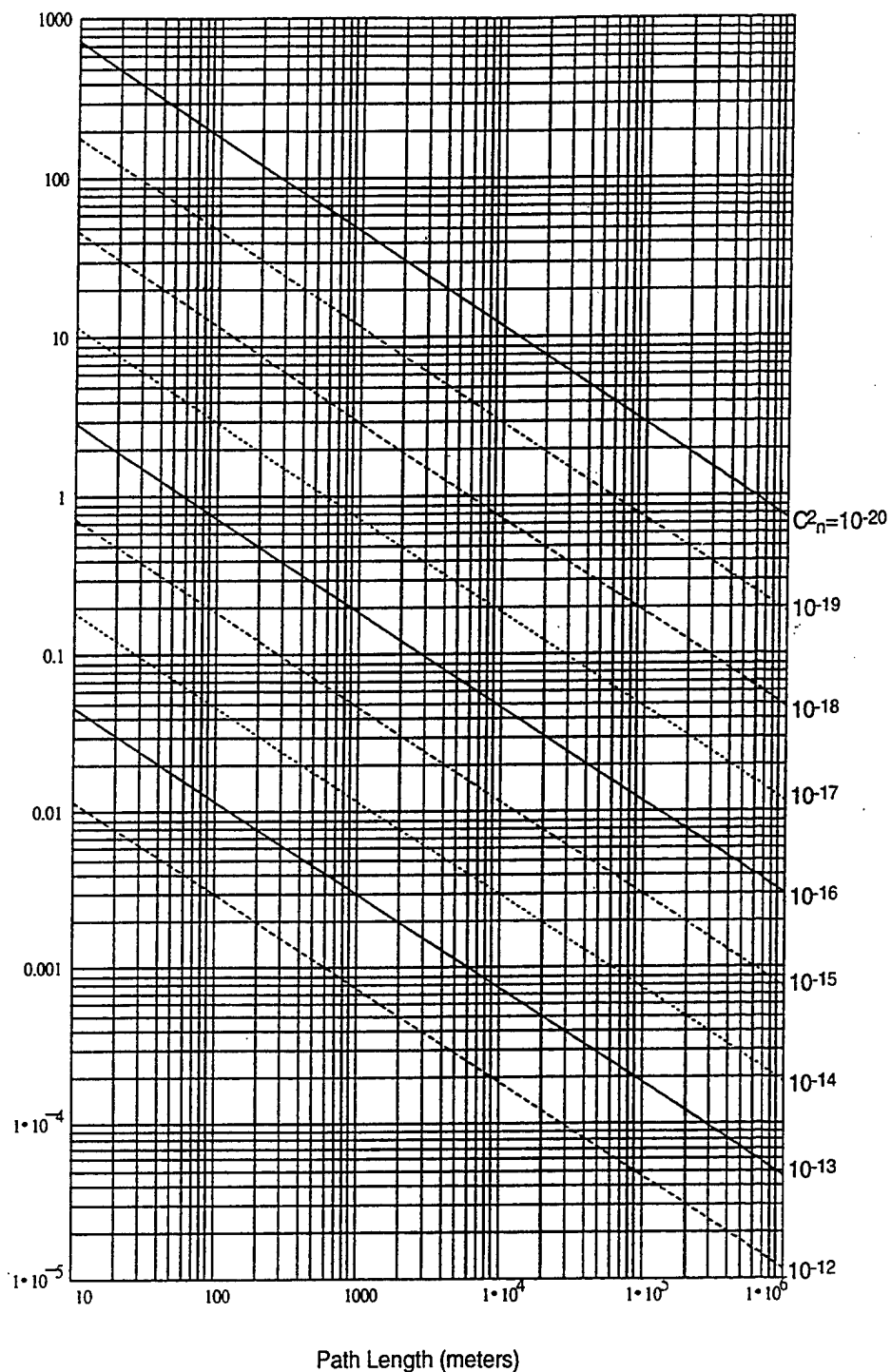


Figure 5-2a. Isoplanatic Patch Diameter vs. Path Length at $0.5 \mu\text{m}$ Wavelength for Various C_n^2 .

Isoplanatic Patch Diameter p_0 (meters)

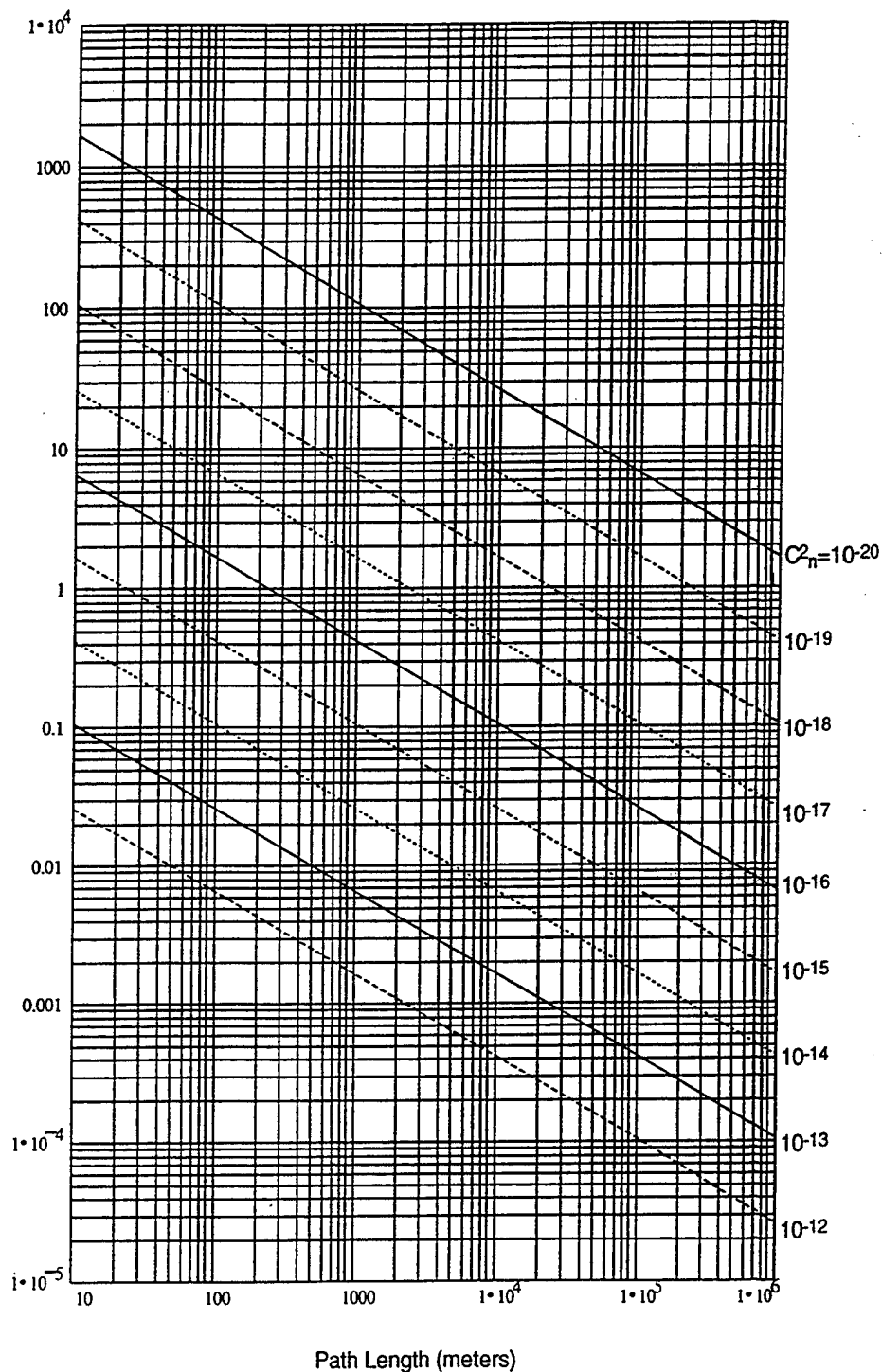
 $\lambda = 1 \cdot 10^{-6}$ meters


Figure 5-2b. Isoplanatic Patch Diameter vs. Path Length at 1.0 μm Wavelength for Various C_n^2 .

Isoplanatic Patch Diameter p_0 (meters)

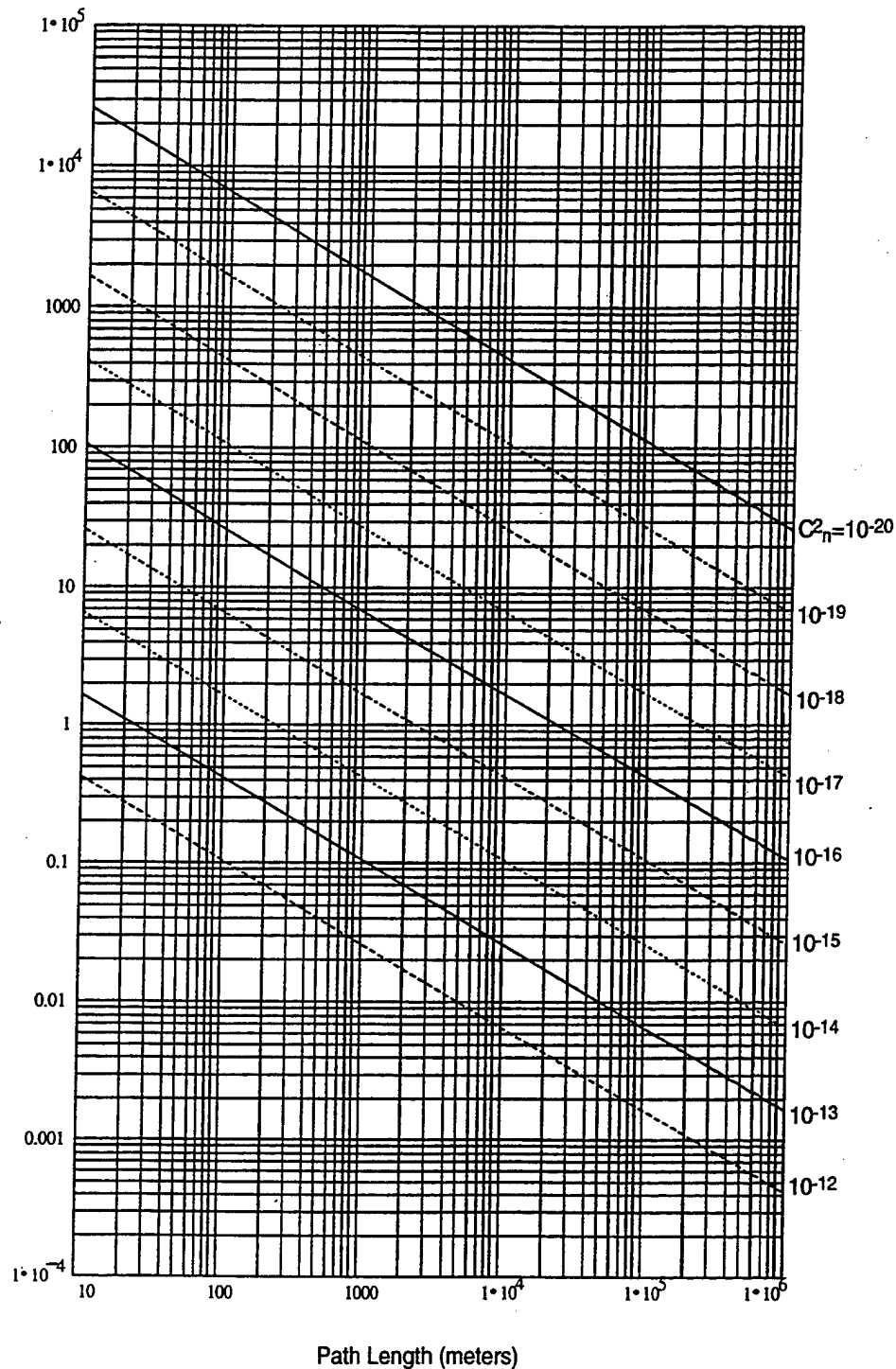
 $\lambda = 1 \cdot 10^{-5}$ meters


Figure 5-2c. Isoplanatic Patch Diameter vs. Path Length at 10 μ m Wavelength for Various C_n^2 .

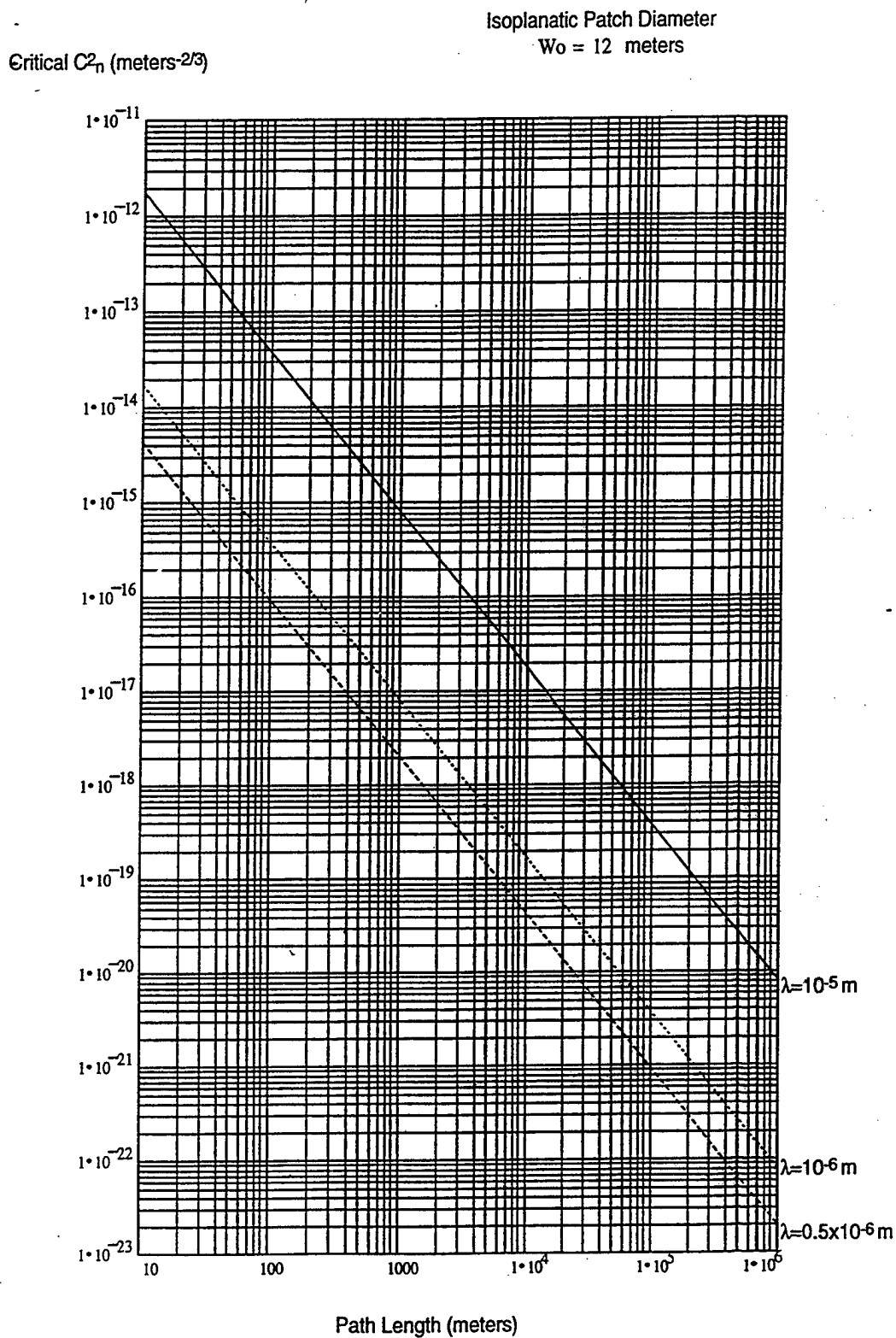


Figure 5-3. Critical C_n^2 for an Isoplanatic Patch Diameter of 12 m vs. Path Length for Various Wavelengths.

6 ISTEf EXPERIMENTAL DESIGN

The objective of this proposed plan is to experimentally demonstrate at BMDO/ISTEF (Ballistic Missile Defense Organization Innovative Science and Technology Experimental Facility) the robustness and sensitivity of speckle based target shape discrimination and motion determination of remote targets. We propose to use ISTEf test ranges, other facilities, and available equipment as much as possible.

Concept

The basic concept is to illuminate a target, such as a missile, with a one pulse or train of coherent laser light pulses and to directly record resulting speckle patterns with a detector array. The conceptual experimental arrangement is illustrated in Figure 6-1.

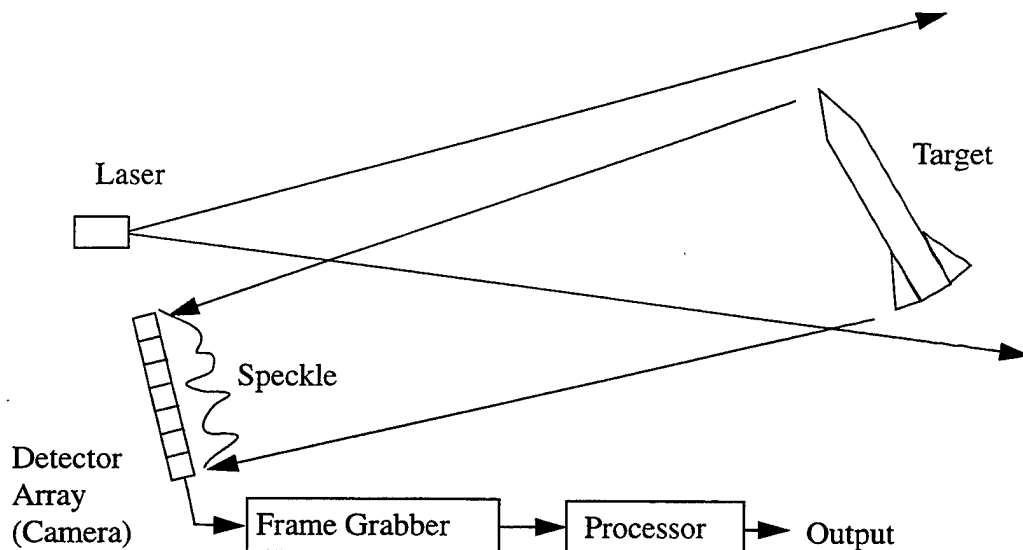


Figure 6-1. The Speckle Based Concept.

Notice that no attempt is made to optically form an image of the target, but instead the intensity (speckle) pattern that is formed from the light scattered from the target is recorded with an electronic camera. By processing the recorded speckle patterns, target shape information and target motion information is obtained. The shape of the speckles

allows us to obtain information about the shape and orientation of the target. The speckle motion allows us to gather information about the target's trajectory and/or rotation rate.

The advantage of using such simple (non-imaging) systems is that detector arrays could be mounted conformally on the surface of an acquisition platform without requiring expensive, heavy, and bulky optics. Also, the processing computational load required to obtain the desired information is small enough to allow real-time operation.

Selection of Experiments

There are a number of possible speckle experiments listed in Table 6.1 that can be

Table 6.1 Potential Experiments

Laser	Detector	Measurements				
		Rotation Rate/ Direction	2- D Shape	3-D Shape	Separation	Vibration
CW	CCD-SF-G	X	X		X	
CW	CCD-MF-G	X	X		X	X
CW-Tunable	CCD-MF-G		X	X	X	
Short Pulse	ICCD-SF		X, E		X, E	
Double Short Pulses	CCD-SF		X		X	
Long Pulse	CCD-SF	X, E	X, E		X, E	
Long Pulse	Double Gated ICCD-SF	X, E				
Double Long Pulses	CCD-SF	X				

Key:

SF - Single Frame, MF - Multiple Frames, G - Gated

CCD - Charge Coupled Detector Array Camera

ICCD - Intensified CCD

X - 1 km Range, E - Eastern Range

carried out based on various types of lasers, cameras, and ranges. The highlighted table cells are experiments that can be accomplished with known ISTEf equipment on either

the ISTEf 1 km laser test range (denoted by X in Table 1) or the Air Force Eastern Range (denoted by E in Table 6.1)[6.1]. The 1 km test range starts at the main site and extends to the north. The Air Force Eastern Range is a nearby facility where the Air Force launches rockets from Cape Canaveral Air Station and at which laser imaging has been accomplished at ranges up to 5 to 7.5 km [6.2].

There are basically 3 different measurements (rotation/motion of a target, 2-D projected shape of a target, and separation between targets) that could be accomplished at the two ranges. Properties of the two available ISTEf lasers of interest are given in Table 6.2 and properties of two available cameras of interest are given in Table 6.3 [6.1].

Table 6.2 Lasers

Parameter/Laser	Short Pulse	Long Pulse
Type	Nd:YAG	Nd:Glass Slab
Pulse Length (nsec)	10	600
Pulse Rep Rate (Hz)	10	3
Energy per Pulse (J)	1.5 at 1064 nm 0.5 at 532 nm	30 at 1054 nm 16 at 527 nm

Table 6.3 Cameras

Parameter/Camera	Sony (2) SSC-D7	Xybion 350 (1)
Detector	Silicon	Gen 2 Intensified
Pixel Size at CCD (μm)	11.5 x 13.4	11.5 x 13.4
Effective Pixel Size at Intensifier Face (μm)	Not Applicable	17.2 x 20.1
Pixel Count	768 x 493	768 x 493
Effective Aperture (mm^2)	8.8 x 6.6	12.7 x 9.6
Intensifier Gain	Not Applicable	300 to 18,000
Minimum Gating Time (ns)	Not Applicable	25
Wavelength Range (μm)	0.4-1.1	0.48-0.88

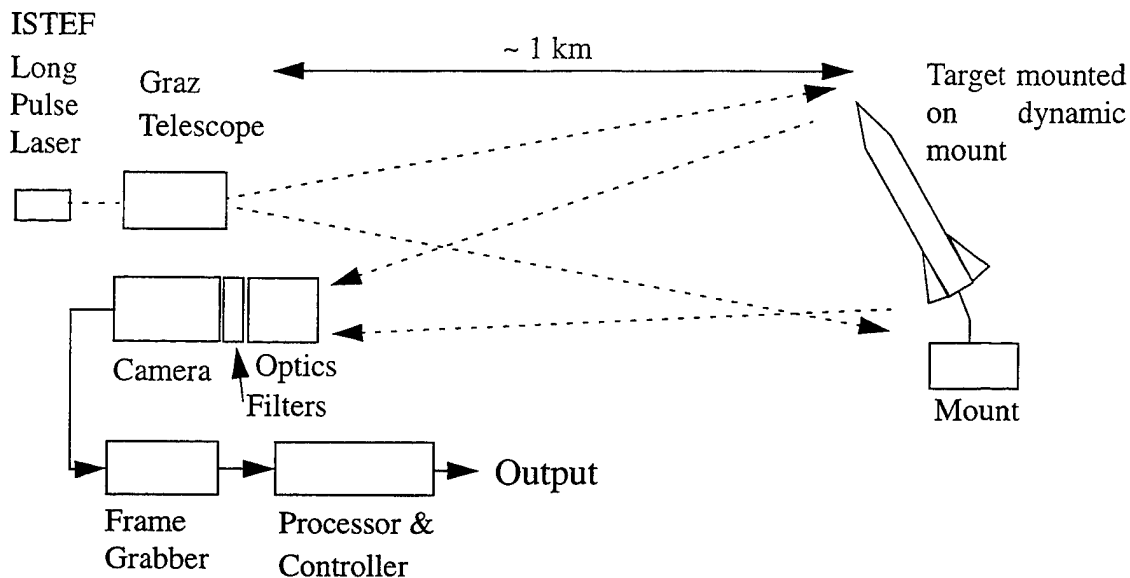


Figure 6-2. The Baseline Experimental Arrangement.

Baseline Experiments

The baseline experimental arrangement is illustrated in Figure 6-2. A full size missile or surrogate (scaled) target is mounted on a pedestal such that it can be rotated in various ways to present dynamic changes in perspective as the experimental data is acquired. A train of coherent laser light pulses illuminate the target. Scattered light from the target for each pulse is captured as a speckle pattern by a digital camera and acquisition system. The relative shape of the target and its motion is obtained by digitally processing the captured train of speckle patterns.

The range could cover short distances (even indoors) with scaled models to long distances with full size targets. It is also possible that actual launched missiles could be tracked and detected by modifying current ISTEFLaser imagers that have been used for imaging the NASA Cassini launch [6.2]. However, our proposed baseline experimental setup is for a full size (~ 0.9 m by 10 m) "scud class" of missile target mounted at a range of 1 km using the ISTEFLaser 1 km range. This allows the speckle based concepts to be evaluated on full sized targets under controlled geometrical conditions.

Source/Transmitter

The baseline light source is the ISTEf Long Pulse Laser. It is a Nd:Glass slab laser that puts out 30 Joules/pulse at 1054 nm or 16 joule/pulse at 527 nm with a pulse length of 600 ns and with a pulse repetition rate of up to 3 pulses per second. The output at the visible wavelength (527 nm) is the baseline wavelength of operation. The pulses are short enough (i.e., < 1 ms) to ensure that the atmospheric turbulence can be considered to be frozen over the exposure time associated with each pulse. Each pulse is to be spatially and temporally coherent with itself such that the entire 3-D target is coherently illuminated during a pulse. However, no coherence between pulses is expected since the pulse rate is too slow for multiple pulses during the atmospheric freeze time.

The Long Pulse Laser can be fed into the Contraves Graz optical tracker mount installed in the tower and dome at the northeast corner of the ISTEf site. The mount has a 20" reflecting telescope operating at f/2 which can operate from the UV through MWIR wavelengths. It has a 2 inch clear aperture Coude feed which has been used to give 532nm and 1064nm illumination for collimated output. To illuminate the entire target the feed will need to be modified to give an expanding beam. However, even partial illumination of the target could produce useful information for the target rotation experiments.

The Long Pulse Laser has the potential to be double pulsed, which could give our experiments more versatility, but this double pulsing modification has not been implemented.

Target

We propose a target for the baseline experiments that is a full-scale mock-up of the scud missile type, or possibly an actual missile. This type of missile has a range of sizes and characteristics as listed in Table 6.4 [6.2]. For analysis and calculation purposes, the nominal baseline experimental dimensions for the missile are taken to be 0.9 m in diameter by 10 m in length.

We plan on two stages of mounts for the target. The first stage is a simple rotation stage to establish some initial results and verify the basic concepts and adequacy of the experimental setup. The second stage requires a more complicated mount on the rotation stage that can move the missile in various ways to generate experiments that produce a greater range of potential sensor-missile operational conditions.

Table 6.4 Scud Missile Properties

Property	Values	Units
Designation	SS-1(A, b, B, c, or C)	US Designations
Length	9.45 to 11.58	m
Diameter	0.76 to 0.914	m
Length/Diameter Ratio	8.3:1 to 14:1	
Max Speed (Cut-off Speed)	1,100 to 1,500	m/sec
Range	160 to 450	km
Wingspan/Fin	0 to 2.9	m

The initial setup stage would be to mount the missile in a vertical position on a rotating table as illustrated in Fig. 6.3a. The table should be elevated to minimize ground turbulence. The missile could be rotated on the table to simulate a spinning missile. Parts of the missile, e.g. the tails, could be changed to different sizes to see if the speckle techniques can distinguish the changes. Multiple targets could also be mounted and illuminated simultaneously to see if they can be sensed by the speckle techniques.

The second stage is where the target is mounted onto a structure that allows three degrees of dynamic rotational freedom in order to allow us to simulate a missile trajectory except for the translation. One rotational axis allows the missile to be rotated about its length axis at a rotation rate of up to 1 revolution per second with up to 5 degrees of offset

to simulate wobble as might occur in actual flight. Another rotational axis (vertical) would allow the missile to turn slowly towards/away from the line of sight directions and the another (horizontal) would allow it to slowly be orientated with different inclinations with respect to the ground plane.

One way of achieving this type of mounting is to attach the missile to two posts, one at each end of the missile. As illustrated in Fig. 6-2b , the posts are mounted on a turn-

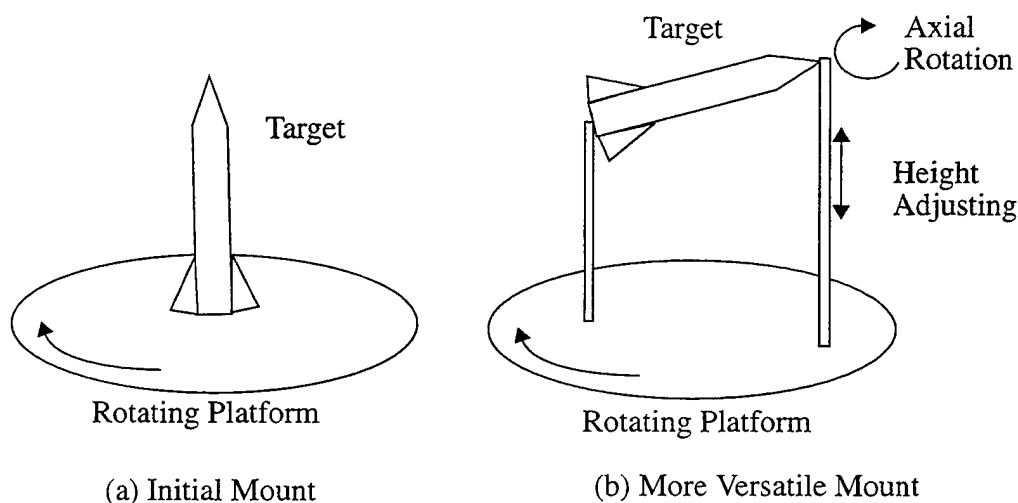


Figure 6-3. Target Mount Assemblies.

table to allow the entire missile to rotate about a vertical axis. Allowing one of the post to be extendable would give the inclination rotation. Rotating the entire missile about its attachment to the post positions would give main rotation about its length axis and if the attachment point to one of the posts is offset from the missile axis then a wobble action would be generated.

We note that a concrete pad with power exists at the end of the 1 km range. However, any mounts for the targets will need to be constructed.

Detector/Receiver

The basic reception process is to detect the speckle patterns with a detector array camera and capture the camera data with a digital frame grabber acquisition system. Con-

ceptually, no lenses are necessary since the speckle pattern at the camera array is the desired quantity to be acquired. However, since we require at least two detectors per speckle for each of the two orthogonal directions, a lens system may be needed to image the speckle pattern on the detector array with correct magnification to properly optimize sampling the speckle pattern. Further, the optics can be used to restrict the field-of-view to help reduce background light detection and hence improve the signal-to-noise ratio. A bandpass filter matching the laser output wavelength is also required to exclude sunlight and other extraneous light in the field-of-view. A polarization filter may also be added to study polarization influences on the techniques.

For our baseline experiments we plan to detect the speckle pattern using the ISTEf Xybion 350 Camera with its own mount near the support building such that the indoor acquisition and processing equipment can be used. The camera is an intensified CCD detector type with 768×493 pixels and with an aperture size of 12.7 mm by 9.6 mm. It is a gated camera that can be operated to expose only during the time the laser pulse is returning from the target. Thus, the background light during other times than during the exposure will not be detected. Appendix C shows a MathCad calculation sheet with the basic equations and parameters for the baseline experiments. With the indicated parameters we find that the number of photons per speckle is about 6900, which is independent of range since the angular speckle size is only dependent on the target size and operational wavelength and since we assume the illumination beam is adjusted in its width to keep the same light energy on the target. We will use the camera directly with no magnification optics. At a 1 km range we have for the 11:1 aspect ratio target about 3 detectors per speckle in one dimension and about 30 in the orthogonal dimension. This arrangement assumes that the camera aperture with its 12.7 mm width (768 pixels X-direction) is orientated along the short (0.9 m) dimension of the target and the 9.6 mm width (493 pixels Y-direction) is orientated along the long dimension (11 m) of the target. With this arrangement the calculations in Appendix C give that there are more than 32 photons per detector element for each laser pulse. The camera intensifier can give a gain of over 15,000. Hence, a large number

of photoelectron events and hence significant output voltage per pixel can be generated even for a few laser photons per pixel.

An additional advantage of using the Xybion camera is that it can be gated twice during the laser pulse time of 600 ns. Thus, if the target is rotating we can obtain two exposures before the atmosphere has changed significantly and demonstrate how the speckle translation can be used to calculate the motion of the target. Given the arrangement described above with no magnification, we have about 22 speckles across the aperture in the X-direction. If we use two 25 ns exposures 500 ns apart and a maximum speckle translation of 11 pixels, we can measure a rotation rate of up to about 1 revolution per second for the target. The smear is only about half a pixel width. Even though we have about 3 laser photons per pixel to work with, there are at least 189312 pixels outputs to generate a correlation. Thus, these experimental conditions are reasonable. Variations in aperture exposure time and separation give additional experimental latitude.

Timing equipment to synchronize the camera with the laser pulses and the target mount will need to be assembled. We plan to interface with the ISTEFP9527 Image Processor and real-time disk array system to digitize and store the acquired data.

Processing

The basic processing for missile typing is to autocorrelate the speckle pattern obtained from each laser pulse and/or take the Fourier Transform of the speckle pattern to get a direct estimate of the autocorrelation of the complex valued target amplitude. From the autocorrelation we can measure the shape of the main lobe, which is related to the shape of the object. From the speckle Fourier Transform we can examine the object autocorrelation. If the target is not changing its shape significantly, e.g., it is keeping its same profile to the line of sights, the correlations from the various pulses can be summed to improve the overall signal-to-noise ratio and improve the shape discrimination. When there are double exposures on the same frame the autocorrelation generates a secondary set of peaks. Measuring this spacing between the secondary peaks and knowing the exposure separation time will give the speckle translation rate.

Initial processing would be done on stored experimental data with available ISTEf computers or with off-site computers in order to refine the processing algorithms using actual acquired data. Subsequently, real-time processing with the ISTEf DVP (Digital Video Processor) or other computers accessing the RTD (Real-Time Disk) array would be demonstrated.

Issues

There are a number of technological issues to be investigated as part of the experiments. They include the following.

Spatial and temporal coherence of the Long Pulse Laser: The coherence characteristics of the source laser will need to be known to understand its impact on the speckle formation. It is our understanding that coherence properties of the long pulse laser under consideration have not been experimentally tested. Partial coherence can reduce the contrast of the speckle and its desired information content. Thus, measurements of the lasers output signal, including its temporal and spatial coherence, will be carried out early in the program in order to help determine the exact nature of subsequent speckle experiments.

Depolarization of the scattered light by the target: Depolarization of the laser light due to scattering by the target adds to the complexity of the speckle pattern. Polarizers may be required at the detector to enhance discrimination. Experience with the targets of interest will help resolve this issue.

Atmospheric effects via the illumination beam: Beam breakup can change the shape of the speckle and beam tilt can translate the speckles. It may be necessary to monitor the atmospheric conditions to keep track of the severity of these effects and relate the conditions to the experimental results.

Atmospheric effects via the scattered wavefront: The stability of the speckle pattern is affected by the atmospheric conditions. For single short pulse operation many of the low-level distortion atmospheric time effects are not significant. However, if severe atmospheric distortions are typically present it may be necessary to monitor the atmospheric conditions to keep track of the severity of these effects and relate the conditions to the experimental results.

Detector noise and photon noises: Noise limits the fundamental sensitivity of the speckle measurement techniques. We expect these limitations will be quantified as the experiments progress and the level of the noise sources is established.

Target skin scattering characteristics: The target bidirectional scattering profile will influence the speckle size and shape for 3-D objects such as a cylindrical missile. Specular reflections reduce the strength of the speckle formation and glints could saturate the detector. Experiments with the targets of interest will allow these effects to be evaluated and incorporated as part of the speckle analysis.

Feature shapes on the target: The requirements for useful speckle discrimination of three dimensional shapes and features is not clear. Further analysis and experimental verification would be carried out.

Micro-motions of the target during the pulse: Micro-vibrations of the target driven by the mount motion or wind could affect the speckle techniques. We will assess minimizing vibrations during the design of the mounts and how the experiments are run. However, such vibrations might be a benefit if they help characterize the target via their impact on the speckle.

Effect of detector spatial and temporal responses: Non-uniformity of detector pixel responses could affect measurement accuracies. Typically, these errors can be corrected with post-detection processing.

Multiple targets with different motion: Multiple motion targets simultaneously in the field of view complicates the analysis of the speckle pattern. We are not initially addressing this effect since we will have a simple target set. Further analysis will need to be carried out to understand the discrimination of the speckle techniques under these conditions.

Linearity of ICCD Camera: Intensity non-linearity response and saturation of the camera intensifier may affect the processing of the data. Typically, such point non-linearity can be corrected with post-processing, but saturation should be avoided.

References

- [6.1]. A. T. Textoris, ISTEf Site Capabilities and Guide for Visiting Experiments, April, 1995.
- [6.2]. J. Stryjewski, Laser Imaging of Spacecraft Launches Offers High-Contrast Video, OE Reports, No. 160, April 1997.
- [6.3]. R. Foresberg, World Weapon Database, Vol. 1, 1986.

7 TRACKING VIA SPECKLES

Introduction

Three techniques are presented here for tracking a laser illuminated target from its speckles. All the techniques depend on measuring the speckle motion to infer target motion. One technique uses two or more short exposures of the speckles by a detector array. Comparison (i.e., correlation) of the exposures determines the movement of the speckle pattern. The second technique uses a single long exposure which produces speckle streaking from which the speckle motion can be determined. The third technique uses a comparison between continuous time-detection signals from many spatially distributed detectors to establish the speckle motion.

Double Exposure Tracking

In double exposure tracking we take short exposures of the speckles generated by coherently illuminating a translating/rotating target. Either the technique of double pulsing the laser or gating the detector can be used to produce two time-separated exposures. Each exposure can be a separate frame, or for simplicity of hardware, both exposures can be recorded (summed) onto the same frame of the camera. The movement of the speckle pattern can be measured from the autocorrelation of the of the summed pattern on the frame or by cross-correlation of the separately exposed frames. If the two speckle patterns are only translated versions of the same pattern, then a local correlation peak indicates the projected speed and direction (velocity) of the speckles.

The speckle motion is caused by relative angular change (rotation) between the target and the source and detectors. In general, the expression for speckle motion depends on not only the geometry and relative motions of the scenario, but also on the wavefront generated by the optics [7.1-7.4]. For far-field operation in a monostatic system where the source and detectors are co-located the speckle velocity is given by

$$V = 2 \cdot \Omega \cdot R \cdot \sin \alpha \quad (7.1)$$

where Ω is the instantaneous angular rotation rate of the source/detector as seen from the target, R is the range to the target, and α is the angle between the line-of-sight and the orientation of the rotation axis. See Figure 7-1. Thus, we see from the equation that knowing

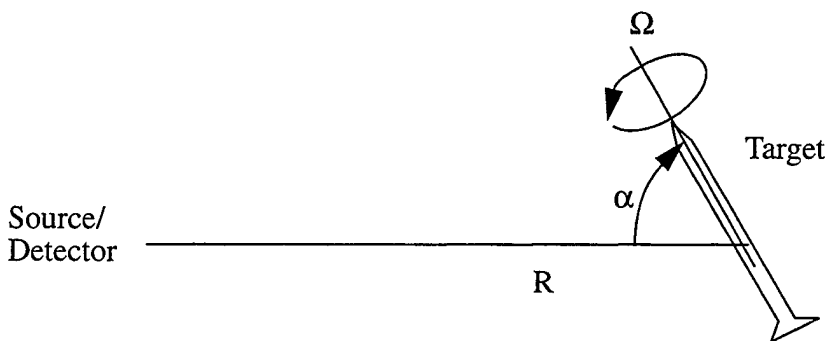


Figure 7-1. Rotation Geometry.

just the speckle velocity does not allow us to directly distinguish between the range, rotation rate, and tilt angle. Additional information such as range information and trajectory dynamics might allow us to obtain the specific information, e.g., rotation rate or tilt that we seek.

The movement of the speckles between exposures must be less than the aperture width for any correlation to be achieved. We pick that the total speckle translation be less than half the aperture width A as given by

$$V_{speckle} \cdot \Delta T \leq \frac{A}{2} \quad (7.2)$$

where ΔT is the time between exposures and $V_{speckle}$ is the speckle translation velocity. If we use $R \cdot \sin \alpha = 100$ km, $\Omega = 1$ revolutions per second, and $A = 30$ cm, then ΔT needs to be less than 120 nsec.

Decorrelation of the speckle pattern occurs as the target rotates. The decorrelation angle depends on the geometry and the target shape. For a cylinder the decorrelation angle is given by [7.5]

$$\varepsilon = \left(\frac{2\lambda}{L} \right)^{\frac{1}{2}} \quad (7.3)$$

where, L is the diameter of the cylinder. Thus, realizing that the angular speckle size is given by λ/L , we see that the decorrelation distance d in term of speckle widths is given by

$$\frac{d}{\sigma_{speckle}} = \frac{2\varepsilon}{\lambda/L} = \left(\frac{8L}{\lambda} \right)^{\frac{1}{2}} \quad (7.4)$$

For $L = 0.76$ m and $\lambda = 0.5$ μm the above expression gives a value of 3487. We would typically expect the number of detectors in the array be limited to less than 1000 and with at least 2 detectors per speckle we see that the decorrelation distance is more than adequate.

Speckle Streaking

With the speckle streaking technique, a single long exposure is used to record a streaked speckle pattern. Taking the Fourier transform of this streaked speckle pattern forms a one dimensional ridge that is perpendicular to the speckle motion. Thus, this ridge points in the direction of the projected spin axis and variations of this direction from frame to frame provides information about the angular dynamics of the target. This technique is easier to use than the double exposure technique since it does not require carefully timed exposures. Long exposures for linear speckle translation may smear the resulting speckle too much to give velocity measurements, but will always give the angular direction. Angular accuracy to better than 0.1 degree has been demonstrated [7-6].

Temporal Speckle Motion Detection

Temporal speckle motion detection uses a number of fast detectors that capture the intensity of the speckles moving past them. The detectors are spatially dispersed in an advantageous pattern, e.g., along a circle. By continuously cross-correlating the signals from detectors the direction and speed of the speckle motion can be determined. Although a filled array of detectors is not needed for this technique, a large number (probably >100)

of fast and sensitive (i.e., expensive) detectors as well as a fast correlation processor would be needed.

References

- [7-1]. Marron, J. C., and K. S. Schroeder, Speckle from rough rotating objects, *Applied Optics*, Vol. 27 No. 20, 4279-4287, 15 Oct 1988.
- [7-2]. Okamoto, T. and T. Asakura, The Statistics of Dynamic Speckles, Chapter III in *Progress in Optics XXXIV*, E. Wolf editor, Elsevier Science B. V., 1995.
- [7-3]. Erdmann, J. C., and R. I. Gellert, Speckle field of curved, rotating surfaces of Gaussian roughness illuminated by laser light spot, *J. Opt. Soc. Am.*, Vol. 66 No. 11, 1194-1204, Nov 1962.
- [7-4]. Yoshimura, T., and S. Iwamoto, Dynamic properties of three-dimensional speckles, *J. Opt. Soc. Am. A*, Vol. 10 No 2, 324-328, Feb 1993
- [7-5]. George, N., "Speckle from rough, moving objects," *JOSA*, Vol. 66 No. 11, 1182-1194, Nov 1976.
- [7-6]. Shirley, L. G., et. al, "Advanced Techniques for Target Discrimination Using Laser Speckle," *The Lincoln Lab Journal*, Vol. 5 No. 3, 365-440, Fall 1992

APPENDIX A

Application of Superresolution Algorithm to Optical Coherent Imaging

J.R. Fienup, M.R. Kosek, and H.C. Stankwitz

Environmental Research Institute of Michigan
P.O. Box 134001, Ann Arbor, MI 48113-4001
fienup@erim.org

Abstract

The Super-SVA algorithm has been shown effective for improving the resolution of microwave synthetic-aperture radar (SAR) images.¹ In this paper we review the Super-SVA algorithm and demonstrate its application to optical imaging systems using coherent laser illumination. Examples of such imaging systems include heterodyne-array imaging, holographic laser radar, laser synthetic-aperture radar, coherent phase retrieval from pupil-plane intensities, and SCIP (sheared-beam imaging). We consider the case of a bright object on a dark background. We show the difference in performance for different features of the image -- prominent points versus extended, diffuse areas.

In **Proc. SPIE 2827-08 Digital Image Recovery and Synthesis III**, 5-6 August, 1996, Denver, CO.

Application of Superresolution Algorithm to Optical Coherent Imaging

J.R. Fienup, M.R. Kosek, and H.C. Stankwitz

Environmental Research Institute of Michigan
P.O. Box 134001, Ann Arbor, MI 48113-4001
Internet: fienup@erim.org

ABSTRACT

The Super-SVA algorithm has been shown effective for improving the resolution of microwave synthetic-aperture radar (SAR) images.¹ In this paper we review the Super-SVA algorithm and demonstrate its application to optical imaging systems using coherent laser illumination. Examples of such imaging systems include heterodyne-array imaging, holographic laser radar, laser synthetic-aperture radar, coherent phase retrieval from pupil-plane intensities, and SCIP (sheared-beam imaging). We consider the case of a bright object on a dark background. We show the difference in performance for different features of the image -- prominent points versus extended, diffuse areas.

Keywords: Super-resolution, coherent imaging, image processing, sidelobes, bandwidth extrapolation, iterative algorithm

1 INTRODUCTION

The resolution of optical imagery is classically limited by diffraction from the collecting aperture. For many years researchers have sought signal-processing and mathematical approaches to recovering greater detail from collected imagery. Recently a new superresolution technique, Super-SVA,¹ has proven successful for obtaining improved resolution from microwave synthetic-aperture radar (SAR) imagery. In part, it is effective there because, at long wavelengths, cultural objects are highly specular, making point-like scatterers common in microwave SAR. In this paper we explore the efficacy of Super-SVA to optical imagery. This would be applicable to coherent imaging modalities such as heterodyne-array imaging, holographic laser radar,² laser synthetic-aperture radar,³ coherent phase retrieval from pupil-plane intensities,⁴ and SCIP (sheared-beam imaging),⁵ among others. It can also be applied to non-optical imaging modalities governed by a coherent transfer function, such as magnetic resonance imaging (MRI). For these imaging modalities the impulse response is the Fourier transform of the aperture function, rather than the squared magnitude of the Fourier transform of the aperture function.

Even though the coherent optical imaging process may be mathematically equivalent to the SAR imaging process, the superresolution algorithm may not work as well because of the nature of the optical imagery. In particular, at optical wavelengths, objects are less specular, resulting in fewer, if any, point-like image features that are important to the success of Super-SVA. In this paper we show examples of simulated coherent optical images and demonstrate the effectiveness of Super-SVA in obtaining additional resolution from them. We show the difference between objects having specular components and those that are purely diffuse. We begin by reviewing Super-SVA, then show results for the two types of optical images, and discuss the results.

2 SVA AND SUPER-SVA

Before describing Super-SVA, we briefly describe the spatially variant apodization (SVA) algorithm,⁶ the engine that makes it work.

Sidelobes of the impulse response in an image can be controlled by placing a weighting or apodization function over the aperture. However, while weighing down the edges of the aperture does decrease sidelobes, it does so at the expense of widening the main lobe of the impulse response, thereby degrading resolution. SVA circumvents this trade-off, yielding an image of a point source having the fine resolution of an unweighted aperture while having no sidelobes whatsoever. It accomplishes this feat by effectively computing the images from a family of aperture weighting functions, and selecting, on a pixel-by-pixel basis, the image value having the minimum magnitude. Because of the properties of the cosine-on-a-pedestal weighting functions — which includes unweighted, Hamming, and Hanning functions as special cases — this minimization can be done very simply and efficiently from the image computed from an unweighted aperture. The special property that makes this efficiency possible is the fact that the discrete Fourier transform of these weighting functions consists of only three non-zero pixels: the center pixel and two adjacent sidelobe pixels, the values of which are proportional to the coefficient of the weighting function. Hence the images from all the other members of the family of weighting functions can be computed by a simple three-point convolution. We can do this in analytic form and arrive at an expression for the intensity of any given pixel as a function of the weighting-function coefficient. We can also analytically solve for the value of the coefficient that minimizes the intensity at a given pixel. Hence we can efficiently select, on a pixel-by-pixel basis, the weighting function that minimizes the sidelobes at each pixel. The result is a preservation of the narrowest mainlobe from the family of weighting functions but the elimination of sidelobes,⁶ as illustrated in Figure 1 for an image consisting of a single point scatterer.

We see from Figure 1(c) that the result of SVA, in eliminating the sidelobes while preserving the fine-resolution main lobe, is to produce an image that has discontinuous first derivatives. These discontinuities cause the Fourier transform of the SVA image to have energy outside the area of the original aperture, and differ somewhat from the measured data within the original aperture.

These ingredients are all analogous to those employed for the Gerchberg super-resolution algorithm.⁷ For the Gerchberg algorithm we assume that the object being imaged is of finite extent, so we truncate the image to that finite extent, causing a discontinuity that introduces higher-frequency data into its Fourier transform. Then we replace the Fourier transform of that image with the measured Fourier data within the area of the aperture, while keeping the new information at the higher spatial frequencies. We then recompute the image from this extended Fourier transform and repeat the process.

At its most basic level, the Super-SVA algorithm is a modified version of the Gerchberg algorithm, replacing the image-domain support-constraint (truncation) operation by the SVA sidelobe-elimination operation. As iterations progress, more and more energy is added at the higher spatial frequencies outside the aperture, thereby extrapolating the aperture, and achieving improved resolution in the image. Additional details can be found in Reference 1. Super-SVA is effective because SVA injects discontinuities throughout the image rather than just at the edges of the image, thereby creating higher spatial-frequency information in a highly effective manner.

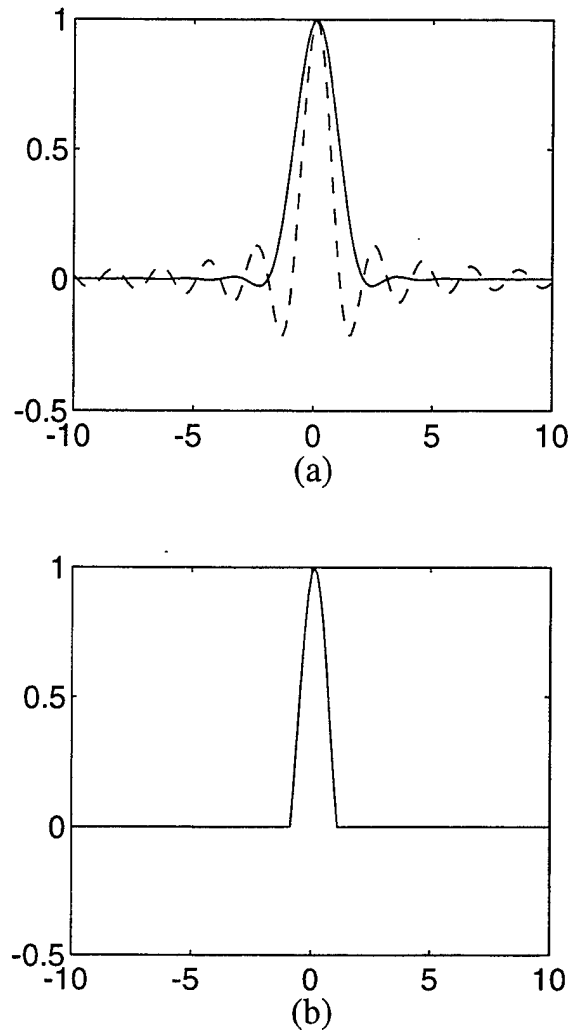


Figure 1. Image of a Point. (a) From unweighted aperture (dashed line) and from Hanning-weighted aperture (solid line), (b) after SVA.

3 SUPER-SVA FOR OPTICAL IMAGERY

Super-SVA works well for microwave SAR imagery, in which bright, point-like scatterers are common. The question that concerns us here is how well might it work for coherent optical imagery, for which specular returns are less common, and sometimes are entirely absent. We answer this question by computer simulation experiments. We start with an incoherent optical image of an object, simulate realizations of speckled, coherent imagery of the object, run Super-SVA, and examine the results. Since subtle details are difficult to discern from a single speckled image, we noncoherently average many images together to reduce the speckle artifacts and more readily discern the difference between the images before and after Super-SVA.

Figure 2 shows the results for our first test object, a photograph of a model of a satellite. This object, made of optically shiny materials, has substantial specular reflections as well as a diffuse component. Figure 2(a) shows the object model. We simulated 36 realizations of coherent speckled

images, each obtained by multiplying the square root of the object by a pure-phase function having a different random phase, then low-pass filtering using a square aperture of length 32 pixels in the Fourier domain. Individual speckled images are difficult to interpret, so we show in each case the noncoherent average of all 36 speckle realizations. The averaging reduces (but does not eliminate) the speckle artifacts. Figure 2(b) shows the original diffraction-limited averaged image, computed from an unweighted aperture. Figure 2(c) shows the averaged image when Taylor weighting was applied to the apertures. It reduces the sidelobes, but at the expense of degraded resolution. Figure 2(d) shows the result of SVA, which has the fine resolution of the image from the unweighted aperture, but without the sidelobes. Figure 2(e) shows the result of Super-SVA, attempting a doubling of the resolution. For comparison we show, in Figures 2(f), the averaged images from an aperture of length 64 pixels, giving true twice-resolution. Comparing 2(e) with 2(b) and 2(f), we see that the Super-SVA image does have finer detail than the original image; and that in the specular point-like areas of the image, the finer detail matches that of the true finer-resolution image. For the diffuse portions of the image, the improvements obtained by Super-SVA are modest, and certainly do not achieve the factor of two improvement seen in the point-like areas of the image.

Figure 3 shows the same things for our second object, a CAD-CAM image of a missile that has no specular returns. Again, SVA greatly reduces the sidelobes, thereby removing the haze in the image around the object. This is a much more difficult case for Super-SVA or for any other superresolution algorithm. In this case, the Super-SVA image does look somewhat sharper than the original diffraction-limited image, but at the price of increasing contrast of the residual speckles in the image. In particular, the point of the missile in the upper-left corner appears sharper than in the original image. The details in the area of the fins in the lower right corner appear slightly sharper as well. However, these effects are subtle enough that they might be difficult to discern in the image reproduced on the page.

Figure 4 shows averaged cuts through the center region of the 32 noncoherently averaged images. The cuts reveal the width of the target. To get a better feel for the width, and to further reduce the effect of the speckles, we averaged over 75 parallel cuts through the center of the image, each shifted appropriately to line up the center of the missile. The top dotted curve shows the given image, with no aperture weighting. The third-from-top dashed curve shows the result of SVA, which is considerably narrower, a marked improvement. The fourth-from-top solid curve shows the result of Super-SVA, a still greater improvement. For comparison, the second-from-top dash-dot curve shows the averaged cuts through the true twice-finer-resolution image (no aperture weighting), and the lowest dotted curve shows the result of SVA on the true twice-finer resolution image. The Super-SVA algorithm reveals an apparent object width that is more consistent with the true twice-finer-resolution image.

4 CONCLUSIONS

We show that SVA and Super-SVA, originally developed for microwave synthetic-aperture radar, also work well for coherent optical imagery. We found that, in the diffuse areas of an image, SVA yields a considerable improvement in image quality over a conventional image, and Super-SVA yields a slight additional improvement. In the specular areas of the image, SVA yields a considerable improvement in image quality over a conventional image, and Super-SVA yields a considerable additional improvement, resulting in a factor-of-two improvement in resolution. Further testing will be required to determine the effects of noise.

On the basis of these results, we recommend the use of Super-SVA on a wide variety of imagery from systems with coherent transfer functions.

ACKNOWLEDGMENTS

This work was supported by the Innovative Science and Technology directorate of the Ballistic Missile Defense Organization, through the Naval Command, Control, and Ocean Surveillance Center RDT&E Division (NCCOSC/NRaD) and the Naval Air Warfare Center (NAWC)

REFERENCES

1. H.C. Stankwitz and M.R. Kosek, "Super-Resolution for SAR/ISAR RCS Measurement Using Spatially Variant Apodization," Proceedings of the Antenna Measurement Techniques Association (AMTA) 17th Annual Meeting and Symposium, Williamsburg, VA, 13-17 November 1995.
2. J.C. Marron and K.S. Schroeder, "Three-dimensional Lensless Imaging Using Laser Frequency Diversity," *Appl. Opt.* 31, 255-262 (1992).
3. C.C. Aleksoff, J.S. Accetta, L.M. Peterson, A.M. Tai, A. Klooster, K.S. Schroeder, R.M. Majewski, J.O. Abshier, and M. Fee, "Synthetic Aperture Imaging with a Pulsed CO₂ TEA Laser," in *Laser Radar II*, Proc. SPIE 783, 29-40 (1987).
4. J.R. Fienup, "Reconstruction of a Complex-Valued Object from the Modulus of Its Fourier Transform Using a Support Constraint," *J. Opt. Soc. Am. A* 4, 118-123 (1987).
5. R.A. Hutchin, "Sheared Coherent Interferometric Photography: A Technique for Lensless Imaging," in *digital Image Recovery and Synthesis II*, Proc. SPIE 2029, 161-168 (1993).
6. H.C. Stankwitz, R.J. Dallaire, and J.R. Fienup, "Non-linear Apodization for Sidelobe Control in SAR Imagery," *IEEE Trans. AES* 31, 267-278 (1995).
7. R.W. Gerchberg, "Super-Resolution through Error Energy Reduction," *Optica Acta* 21, 709-720 (1974).

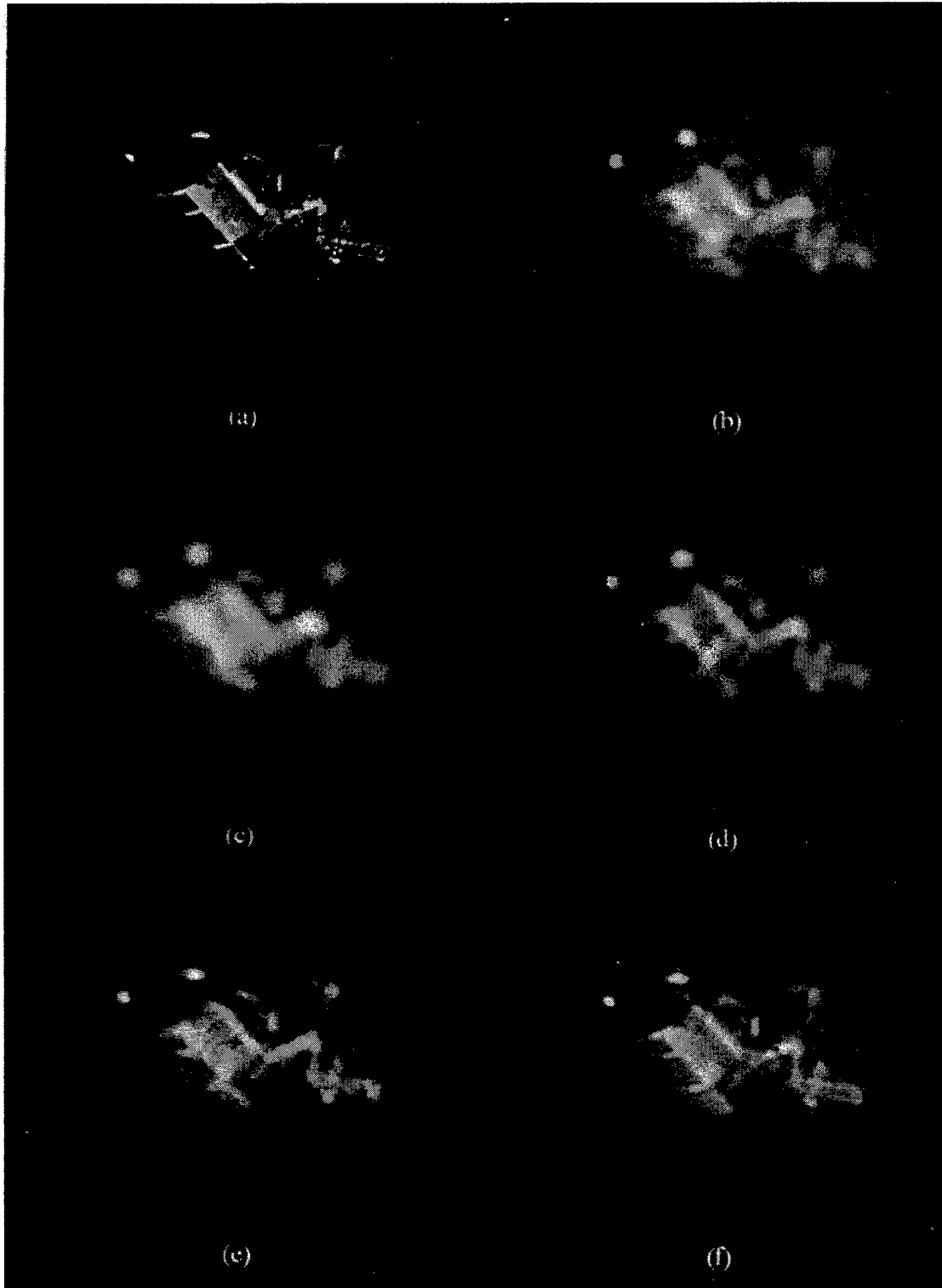


Figure 2. SVA and Super-SVA for Semi-Specular (Satellite) Object. (a) Object model, (b) diffraction-limited image from unweighted aperture, (c) image from Taylor-weighted aperture, (d) result of SVA, (e) result of Super-SVA, (f) image with twice-finer resolution.

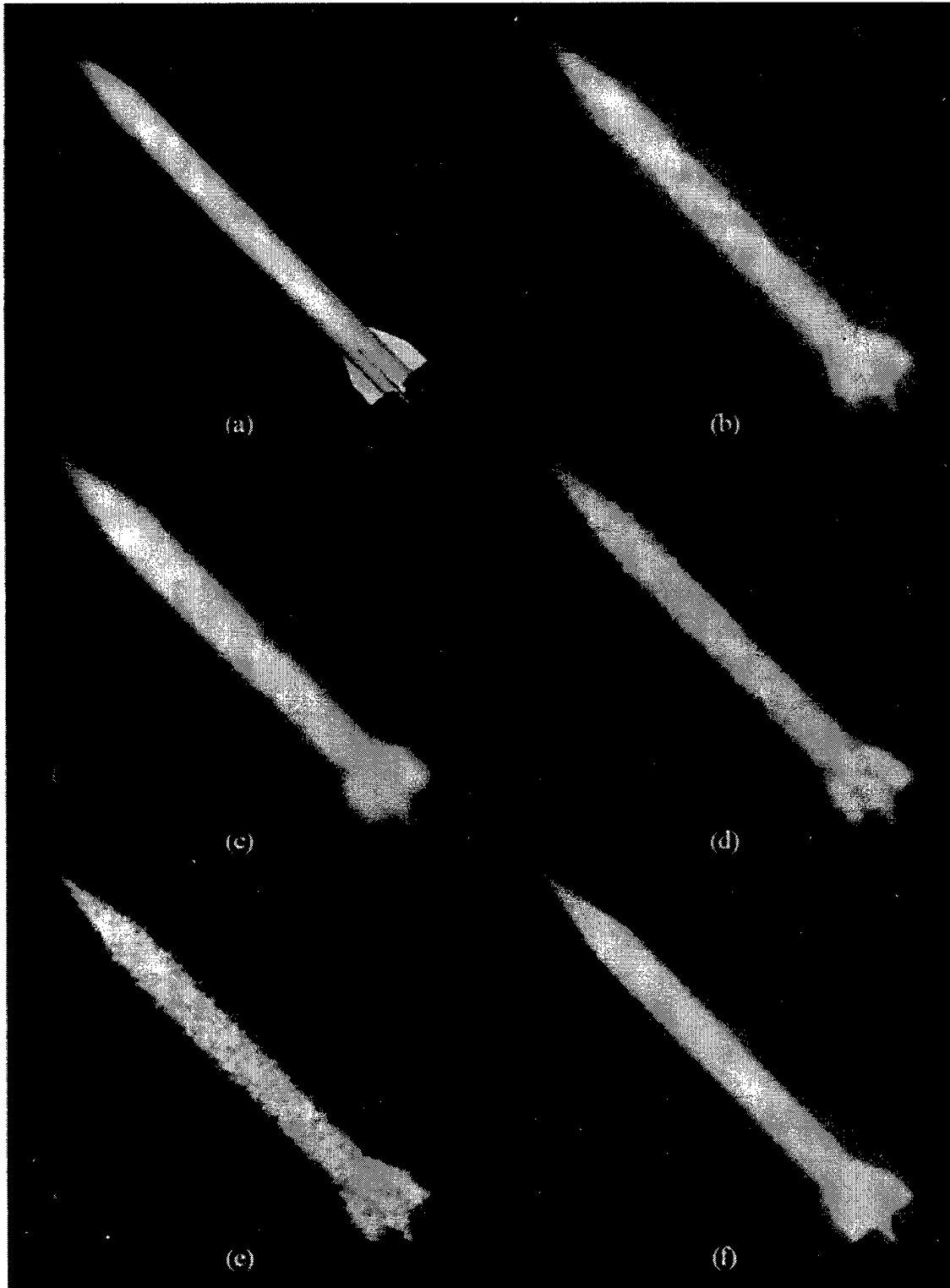


Figure 3. SVA and Super-SVA for Diffuse (Missile) Object. (a) Object model, (b) diffraction-limited image from unweighted aperture, (c) image from Taylor-weighted aperture, (d) result of SVA, (e) result of Super-SVA, (f) image with twice-finer resolution.

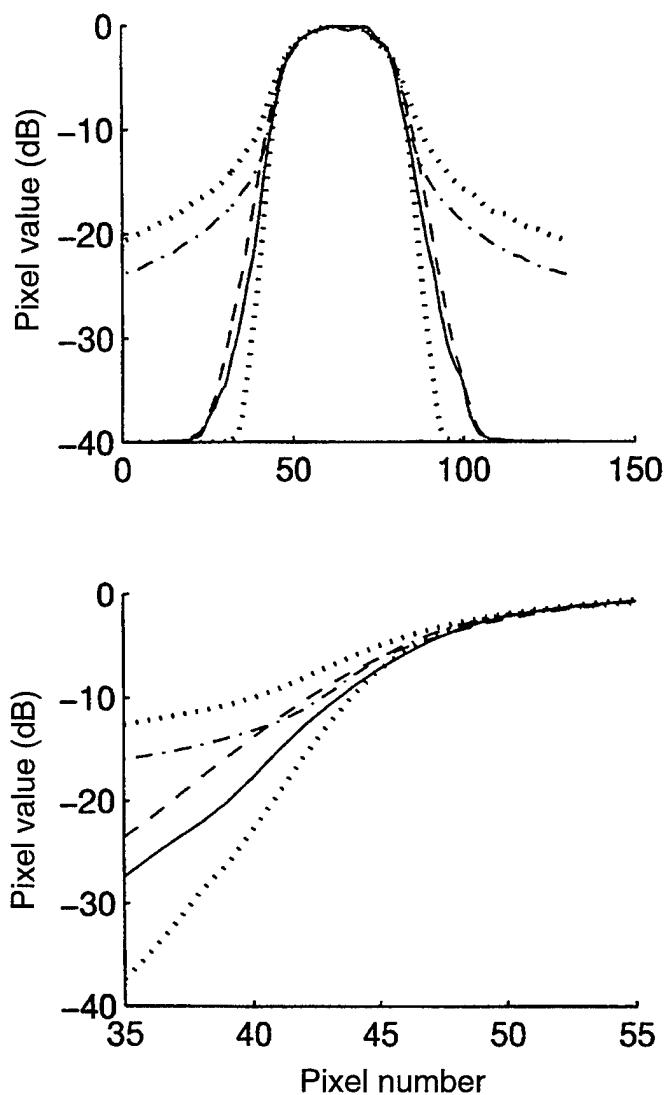


Figure 4. Averaged Cuts through the Missile Image (Log Plots). (a) Over entire width of object; (b) Of left edge of object. Curves (top-to-bottom) represent the given image (····), the true twice-finer resolution image (-.-.), SVA on the original image (- -), Super-SVA on the original image (—), and SVA on the true twice-finer-resolution image (····).

APPENDIX B

Imaging Correlography with Preconditioned Autocorrelation Estimates

Final Report

October 1996

Timothy J. Schulz

**Department of Electrical Engineering
Michigan Technological University
1400 Townsend Drive
Houghton, MI 49931**

Submitted to:

**Environmental Research
Institute of Michigan (ERIM)
Ann Arbor, MI**



Preface

This report documents the results of a study – *Imaging Correlography with Preconditioned Autocorrelation Estimates* – which was performed by Michigan Technological University for the Environmental Research Institute of Michigan during the period July 1995 to September 1996. The principle investigator for this project was Timothy J. Schulz of Michigan Technological University, and the program manager was Dr. James R. Fienup of the Environmental Research Institute of Michigan. Additional support on the project was supplied by S. M. Rathi of Michigan Technological University.

Table of Contents

Preface	i
1 Executive Summary	1
2 Technical Report	2
2.1 Introduction	2
2.2 Object Estimation from Far-Field Intensity Measurements	3
2.3 Preconditioning of the Diffraction-Limited Autocorrelation Estimate in Imaging Correlography	5
2.3.1 Example with Laboratory Data	6
2.3.2 Issues for Further Consideration:	7
2.3.3 Summary	9
Bibliography	10

1 Executive Summary

Autocorrelation estimates obtained in imaging correlography often exhibit large deviations from the truth at low lags. In particular, because the zeroth-lag bias is calibrated by a quantity determined by the data themselves, the zeroth-lag value is often subject to a significant error, especially when few independent speckle frames are available. These errors are important because deviations in the low-lag autocorrelation values from the zeroth-lag value are directly related to a particular measure of object *smoothness*.

The contents of this report include: (i) a brief review of imaging correlography and a discussion of the relationship between object-estimate smoothness and the low-lag values of the corresponding autocorrelation estimate; (ii) a nonlinear clipping method for preconditioning the autocorrelation estimate in an attempt to smooth (or regularize) the resulting object estimate; and (iii) a demonstration of the technique on laboratory data.

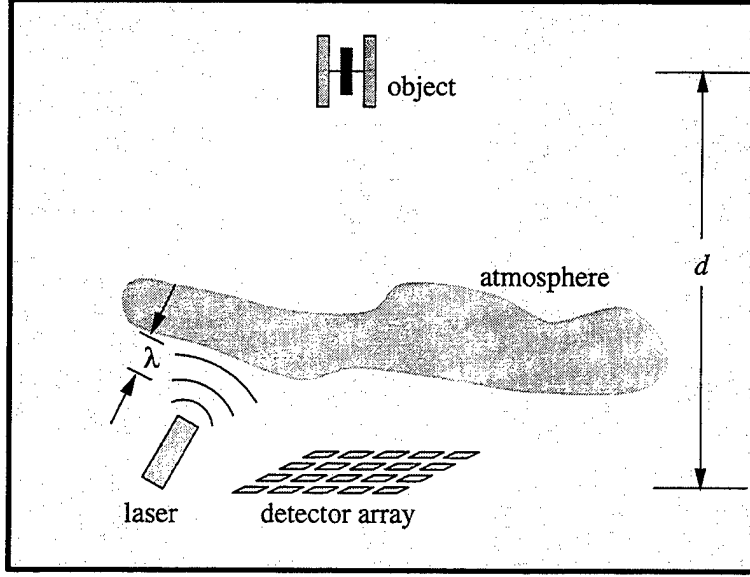


Figure 1: The basic imaging scenario for active laser-illumination.

2 Technical Report

2.1 Introduction

Consider the imaging scenario shown in Figure 1. For a fixed source-object-sensor geometry with coherent plane-wave illumination of the object, the complex amplitude of the field in the detector plane, as discussed by Fienup in [1], can be modeled as

$$g_t(y) = e^{j\theta_t(y)} \int f(x) e^{-j\frac{2\pi}{\lambda d} y \cdot x} dx, \quad (1)$$

where:

- t is an index to time;
- x and y are two-dimensional spatial variables in the object- and detector-planes, respectively;
- $f(x)$ is proportional to the complex amplitude of the field scattered from the object (in the object plane);
- $\theta_t(y)$ is the time-varying phase error introduced by atmospheric turbulence (using the single-layer phase-screen model);
- d is the distance from the object plane to the detector plane; and
- λ is the nominal wavelength of the illumination source.

This is the Fraunhofer far-field propagation model [2] - quadratic phase terms associated with the Fresnel model have been ignored. For fully-developed laser speckle [3], the far-

field complex amplitude $g_t(y)$ is modeled as a zero-mean circular Gaussian process with the covariance function

$$\begin{aligned} E[g_t(y)g_t^*(y')] &= e^{j\theta_t(y)}e^{-j\theta_t(y')} \int o(x)e^{-j\frac{2\pi}{\lambda d}(y-y')\cdot x} dx \\ &= e^{j\theta_t(y)}e^{-j\theta_t(y')} O\left(\frac{y-y'}{\lambda d}\right), \end{aligned} \quad (2)$$

where $o(\cdot)$ is proportional to the incoherent scattering function for the object and $O(\cdot)$ is its two-dimensional Fourier transform. Because $o(\cdot)$ is the far-field power-spectral density in the absence of turbulence-induced phase errors, the estimation of the object's incoherent scattering function $o(\cdot)$ from far-field measurements is a problem of two-dimensional spectrum estimation.

2.2 Object Estimation from Far-Field Intensity Measurements

Measurement of the far-field complex amplitude $g_t(y)$ can be accomplished through holographic, heterodyne, or homodyne methods; however, the short wavelengths associated with visible and infrared radiation make this a difficult and daunting task. A far simpler measurement process, and one that is insensitive to turbulence-induced wavefront errors, is to simply record the far-field intensities:

$$\begin{aligned} I_t(y) &= |g_t(y)|^2 \\ &= \left| \int f(x)e^{-j\frac{2\pi}{\lambda d}y\cdot x} dx \right|^2 \\ &= \left| F\left(\frac{y}{\lambda d}\right) \right|^2, \end{aligned} \quad (3)$$

where $F(\cdot)$ is the two-dimensional Fourier transform of the object-field complex amplitude. Data will, of course, be acquired only over a limited spatial region, and if this region is defined by a binary pupil-function $P(y)$, then the measured data can be modeled as

$$D_t(y) = \left| F\left(\frac{y}{\lambda d}\right) \right|^2 P(y). \quad (4)$$

If the source-object-sensor geometry is slightly perturbed over time, a sequence of independent speckle patterns can be obtained. To indicate this, we let $D_k(\cdot)$ denote the speckle intensity at time t_k , and assume that the collection $\{D_k(\cdot)\}_{k=1}^K$ are statistically independent.

Image estimation from these far-field intensity measurements is called *imaging correlography* [4–6], and most imaging techniques are motivated by the mathematical form for the statistical moments of the measured data:

$$E[D_k(y)] = O(0)P(y), \quad (5)$$

and

$$\begin{aligned} E[D_k(y)D_k(y')] &= E\left[F\left(\frac{y}{\lambda d}\right)F^*\left(\frac{y}{\lambda d}\right)F\left(\frac{y'}{\lambda d}\right)F^*\left(\frac{y'}{\lambda d}\right)\right]P(y)P^*(y') \\ &= \left[O^2(0) + \left|O\left(\frac{y-y'}{\lambda d}\right)\right|^2\right]P(y)P(y'). \end{aligned} \quad (6)$$

Because of these relationships, it has been suggested in [4] that the squared-magnitude of the inverse Fourier transform of the intensity data:

$$|d_k(y)|^2 = \left|\int D_k(y')e^{j2\pi y \cdot y'} dy'\right|^2, \quad (7)$$

be considered as the starting point for an estimate of the scattering function's autocorrelation function from which a phase-retrieval problem then be addressed for the recovery of the scattering function itself. An examination of the first moment of this function clearly reveals this motivation:

$$\begin{aligned} E[|d_k(y)|^2] &= \iint E[D_k(y')D_k(y'')]e^{j2\pi y \cdot (y'-y'')} dy' dy'' \\ &= \iint O^2(0)P(y')P(y'')e^{j2\pi y \cdot (y'-y'')} dy' dy'' \\ &\quad + \iint \left|O\left(\frac{y'-y''}{\lambda d}\right)\right|^2 P(y')P(y'')e^{j2\pi y \cdot (y'-y'')} dy' dy'' \\ &= O^2(0)|p(y)|^2 + [|p|^2 * r_o](y), \end{aligned} \quad (8)$$

where $p(\cdot)$ is the inverse Fourier transform of the pupil function, $*$ denotes the convolution operator, and

$$r_o(y) = \int \left|O\left(\frac{y'}{\lambda d}\right)\right|^2 e^{j2\pi y \cdot y'} dy', \quad (9)$$

is related (through a scaling of the spatial variable y) to the autocorrelation of the object's incoherent scattering function $o(\cdot)$. Because $|p|^2(\cdot)$ is the incoherent point-spread function for a diffraction-limited imaging system with the pupil function $P(\cdot)$, the function $[|p|^2 * r_o](\cdot)$ is referred to as the *diffraction-limited* autocorrelation of the object's scattering function. Furthermore, because

$$\left|E\left[\int D_k(y')e^{j2\pi y \cdot y'} dy'\right]\right|^2 = O^2(0)|p(y)|^2, \quad (10)$$

an estimate of the diffraction-limited object autocorrelation has been suggested as [4]:

$$\hat{r}_o(y) = \frac{1}{K} \sum_{k=1}^K \left| \int D_k(y')e^{j2\pi y \cdot y'} dy' \right|^2 - \left| \int \left[\frac{1}{K} \sum_{k=1}^K D_k(y') \right] e^{j2\pi y \cdot y'} dy' \right|^2, \quad (11)$$

which has the expectation value:

$$E[\hat{r}_o(y)] = \frac{K-1}{K} [|p|^2 * r_o](y). \quad (12)$$

Although the estimate $\hat{r}_o(\cdot)$ can be used as the data for a phase-retrieval [7, 8] or image recovery from correlations [9] problem, low-lag values of these data often have a relatively low signal-to-noise ratio (SNR). As is shown in the following section, widely discrepant values at low-lags of an autocorrelation estimate can, and usually do, lead to very noisy (or rough) object estimates. For this reason, in the following section we also propose a “clipping” method whereby the autocorrelation estimate $\hat{r}_o(\cdot)$ is preconditioned so that its low-lag elements are close (or equal) in value.

2.3 Preconditioning of the Diffraction-Limited Autocorrelation Estimate in Imaging Correlography

Consider the following measure of *smoothness* for a two-dimensional, discrete image:

$$\mathcal{S}_o(\Delta_x) = \sum_x [o(x) - o(x - \Delta_x)]^2, \quad (13)$$

where Δ_x is some predetermined lag. If, for instance, $\Delta_x = (0, 1)$, then $\mathcal{S}_o(0, 1)$ would represent the smoothness as measured through the intensity differences for adjacent pixels in the second image dimension. An interesting relationship between this smoothness measure and the image’s autocorrelation function is developed as follows:

$$\begin{aligned} \mathcal{S}_o(\Delta_x) &= \sum_x [o(x) - o(x - \Delta_x)]^2 \\ &= \sum_x o^2(x) + \sum_x o^2(x + \Delta_x) - 2 \sum_x o(x)o(x + \Delta_x) \\ &= 2[r_o(0) - r_o(\Delta_x)], \end{aligned} \quad (14)$$

where

$$r_o(y) = \sum_x o(x)o(x + y) \quad (15)$$

is the autocorrelation function for the image. Therefore, $\mathcal{S}_o(\Delta_x)$ can be equivalently expressed through the difference in values of the image autocorrelation at lags 0 and Δ_x . If a smoothness measure over various lags is desired, then a global image smoothness might be defined as

$$\mathcal{S}_o = \sum_l \alpha_l \mathcal{S}_o(\Delta_{xl}), \quad (16)$$

where α_l is the relative weight given to the smoothness in the direction of the l th lag. This quantity is then related to the image autocorrelation according to

$$\mathcal{S}_o = 2 \left\{ \left[\sum_l \alpha_l \right] r_o(0) - \sum_l \alpha_l r_o(\Delta_{xl}) \right\}. \quad (17)$$

Evidently then, images that have small variations between adjacent pixels should also have small variations between low-lag autocorrelation values.

One method for constraining low-lag values of the intensity function to be close in

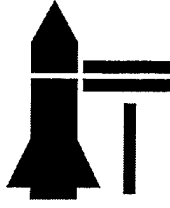


Figure 2: General pattern for the object scattering function used to generate the laboratory data.

value to the zero-lag value is to simply apply the following nonlinear processing to an autocorrelation function estimate:

$$\tilde{r}_o(y) = \begin{cases} \sum_l \alpha_l \hat{r}_o(y) / \sum_l \alpha_l, & y \in \mathcal{Y} \\ \hat{r}_o(y), & y \notin \mathcal{Y} \end{cases}, \quad (18)$$

where \mathcal{Y} is a set of low-lag pixel values and $\{\alpha_l\}$ is a set of weights used for averaging. Another method is to simply clip the central values of the autocorrelation estimate to a constant value.

In summary,

the techniques described in this section should not be interpreted as methods for improving the autocorrelation estimate, but rather as methods for regularizing the resulting intensity estimate. In essence, low-lag values of the autocorrelation estimate are used to enforce smoothness of the object estimate, whereas the large-lag values are used to recover the object structure.

2.3.1 Example with Laboratory Data

Laboratory data acquired by the Environmental Research Institute of Michigan (ERIM) were processed by the techniques described in the previous section. These data were acquired by illuminating a pattern of retro-reflective tape on glass in a configuration similar to the one shown in Figure 2. The data we processed represent data acquired over a region sampled by a 128×128 uniform-grid array. The autocorrelation estimates obtained according to Eq. (11) are shown in Figure 3 for 30, 20, and 10 independent speckle realizations. One can clearly see the problems with the central lag in these autocorrelation estimates. As discussed previously, this error will lead to excessively noisy estimates.

The autocorrelation estimates can be modified by applying the following thresholding operation:

$$\tilde{r}_o(y) = \begin{cases} r_{\max}, & \hat{r}_o(y) \geq r_{\max} \\ \hat{r}_o(y), & \hat{r}_o(y) < r_{\max} \end{cases}, \quad (19)$$

where $r_{\max} = \beta \max_y \{\hat{r}_o(y)\}$ is a percentage (determined by β) of the maximum value

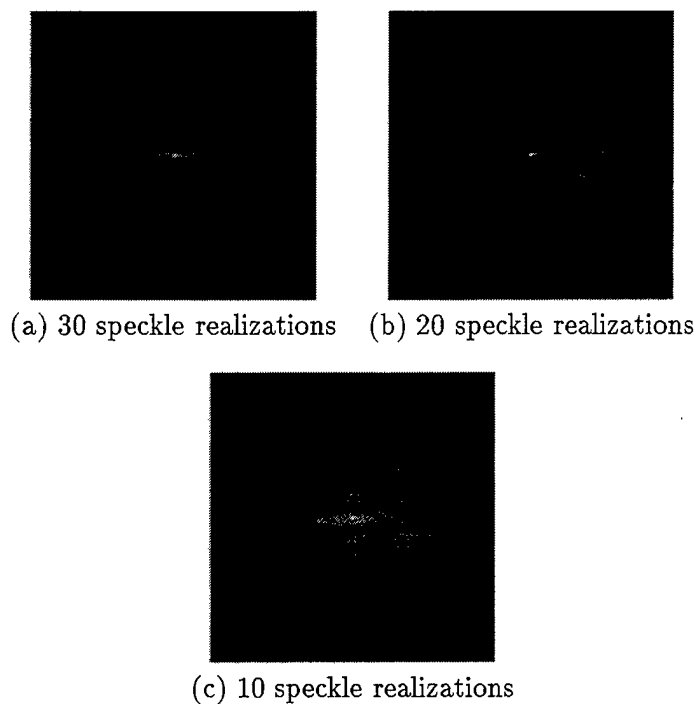
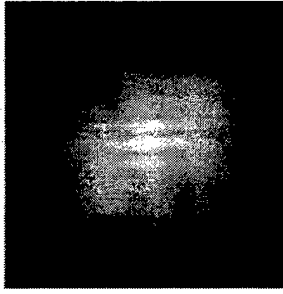


Figure 3: Autocorrelation estimates obtained from the laboratory data according to Eq. (11) for (a) 30, (b) 20, and (c) 10 speckle realizations.

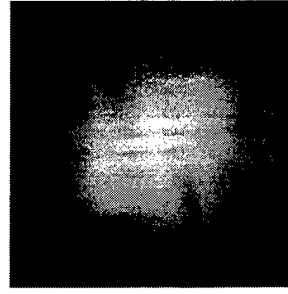
attained over the autocorrelation estimate obtained according to Eq. (11). The modified estimates obtained in this way are shown in Figure 4; the scale factor used was: $\beta = 0.10$ for 10 realizations; $\beta = 0.06$ for 20 realizations; and $\beta = 0.07$ for 30 realizations. The object estimates obtained from these autocorrelation estimates by using the method proposed by Schulz and Snyder in [9] are shown in Fig. 5. The object estimates have been convolved with the diffraction-limited point-spread function for the imaging system $|p|^2(\cdot)$.

2.3.2 Issues for Further Consideration:

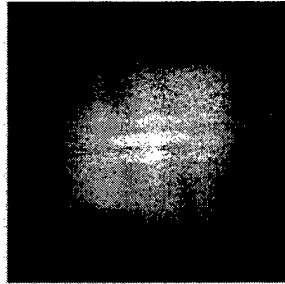
Whereas we have established a link between the low-lag autocorrelation values and object smoothness, the methods proposed here for preconditioning the autocorrelation estimate have not been proven optimal in any sense, and other methods might (and likely will) produce autocorrelation estimates from which better object estimates can be recovered. Additionally, the use of our clipping method requires the selection of a clipping parameter β , and a method for selecting an optimal β has not been addressed. These issues should be considered in greater detail.



(a) 30 speckle realizations ($\beta = 0.07$)

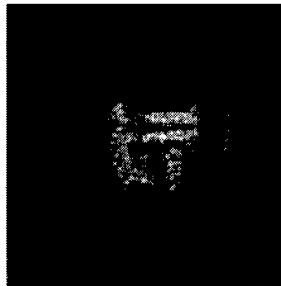


(b) 20 speckle realizations ($\beta = 0.06$)

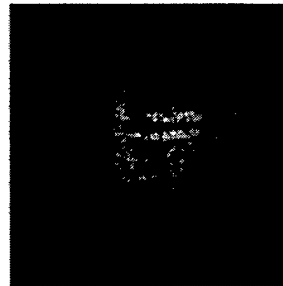


(c) 10 speckle realizations ($\beta = 0.10$)

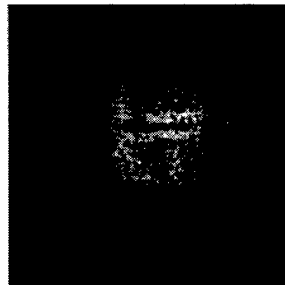
Figure 4: Autocorrelation estimates obtained from the laboratory data according to Eq. (19) for (a) 30, (b) 20, and (c) 10 speckle realizations.



(a) 30 speckle realizations



(b) 20 speckle realizations



(c) 10 speckle realizations

Figure 5: Object estimates obtained from the laboratory data by using the autocorrelation estimates shown in Fig. 4.

2.3.3 Summary

In conclusion, we have presented in this report a motivation and method for preconditioning autocorrelation estimates in imaging correlography. The main motivation lies in the hypothesis that variations in the low-lag values of an autocorrelation function reflect the high-frequency *smoothness* of the corresponding object, and if these values are preconditioned before applying a phase-retrieval procedure, the resulting object estimate will be smoother than one obtained from an unconditioned autocorrelation estimate. In addition, we have presented a simple method for preconditioning, and demonstrated the use of this method on laboratory data.

Bibliography

- [1] J. R. Fienup. Image formation from nonimaged laser speckle patterns. In S. R. Robinson, editor, *The Infrared & Electro-Optical Systems Handbook*, chapter 1, pages 92–109. SPIE Press, 1993.
- [2] J. W. Goodman. *Introduction to Fourier Optics*. McGraw-Hill, New York, 1968.
- [3] J. W. Goodman. Statistical properties of laser speckle patterns. In J. C. Dainty, editor, *Laser Speckle and Related Phenomena, 2nd Edition*, pages 9–75. Springer-Verlag, Heidelberg, 1984.
- [4] P. S. Idell, J. R. Fienup, and R. S. Goodman. Image synthesis from nonimaged laser-speckle patterns. *Opt. Lett.*, 12:858–860, 1987.
- [5] J. R. Fienup and P. S. Idell. Imaging correlography with sparse arrays of detectors. *Opt. Eng.*, 27:778–784, 1988.
- [6] D. G. Voelz, J. D. Gonglewski, and P. S. Idell. Image synthesis from nonimaged laser-speckle patterns: Comparison of theory, computer simulation, and laboratory results. *Appl. Opt.*, 30(23):3333–3344, 1991.
- [7] J. R. Fienup. Reconstruction and synthesis applications of an iterative algorithm. In *SPIE Vol. 373 Transformations in Optical Signal Processing*, pages 147–160, 1981.
- [8] J. R. Fienup. Phase retrieval algorithms: a comparison. *Appl. Opt.*, 21(15):2758–2769, 1982.
- [9] T. J. Schulz and D. L. Snyder. Image recovery from correlations. *J. Opt. Soc. Am. A*, 9:1266–1272, 1992.

Appendix C: Speckle/Photons Calculations

This MathCad worksheet calculates the number of photons per speckle and pixel, and the size of the speckle as a function of range.

Various parameters to be specified are:

$$\lambda := 0.527 \cdot 10^{-6} \cdot \text{m} \quad h := 6.6256 \cdot 10^{-34} \cdot \text{joule} \cdot \text{sec} \quad c := 3 \cdot 10^8 \cdot \frac{\text{m}}{\text{sec}}$$

$$E_{\text{photon}} := \frac{h \cdot c}{\lambda} \quad \text{Photon Energy} \quad E_{\text{photon}} = 3.7717 \cdot 10^{-19} \cdot \text{joule}$$

$$J := 16 \cdot \text{joule} \quad \text{Source Energy per Pulse}$$

$$L_{\text{tx}} := 0.9 \cdot \text{m} \quad L_{\text{ty}} := 11 \cdot \text{m} \quad \text{Target Dimensions}$$

$$A_t := L_{\text{tx}} \cdot L_{\text{ty}} \quad \text{Target Area}$$

$$\rho := 0.1 \quad \text{Target Reflectivity}$$

$$\Gamma := 4 \cdot \rho \cdot A_t \quad \text{Target Cross Section (Simple Diffuse Model)} \quad \Gamma = 3.96 \cdot \text{m}^2$$

$$D_{\text{xrec}} := 0.0127 \cdot \text{m} \quad \text{Effective X-Direction Receiver Width}$$

$$D_{\text{yrec}} := 0.0096 \cdot \text{m} \quad \text{Effective Y-Direction Receiver Width}$$

$$A_{\text{rec}} := D_{\text{xrec}} \cdot D_{\text{yrec}} \quad \text{Aperture Area of Receiver}$$

$$K_{\text{elec}} := 0.6 \quad \text{Photon-to-Electron Conversion Factor}$$

$$K_{\text{fill}} := 0.9 \quad \text{Detector Array Fill Factor}$$

$$N_{\text{x_pix}} := 768 \quad \text{Number of Detector Pixels in x direction}$$

$$N_{\text{y_pix}} := 493 \quad \text{Number of Detector Pixels in y direction}$$

$$\eta_{\text{atm}} := 0.9 \quad \text{Atmospheric One Way Transmission Factor}$$

$$\eta_{\text{trans}} := 0.9 \quad \text{Optical System Transmitter Efficiency}$$

$$\eta_{\text{rec}} := 0.9 \quad \text{Optical System Receiver Efficiency}$$

$$\eta_{\text{pol}} := 0.5 \quad \text{Polarization Factor}$$

$$K_{\text{tx}} := 2 \quad \text{X-direction Transmit Beam Overfill Factor}$$

$$K_{\text{ty}} := 2 \quad \text{Y-Direction Transmit Beam Overfill Factor}$$

$$\theta_{\text{tx}}(R) := \frac{K_{\text{tx}} \cdot L_{\text{tx}}}{R} \quad \text{X-Direction Transmit Beam Divergence Angle}$$

$$\theta_{\text{ty}}(R) := \frac{K_{\text{ty}} \cdot L_{\text{ty}}}{R} \quad \text{Y-Direction Transmit Beam Divergence Angle}$$

$$S_x(R) := \frac{\lambda \cdot R}{L_{\text{tx}}} \quad \text{X- Direction Speckle size}$$

$$S_y(R) := \frac{\lambda \cdot R}{L_{\text{ty}}} \quad \text{Y- Direction Speckle size}$$

$$Q_x(R) := \frac{S_x(R) \cdot N_{\text{x_pix}}}{D_{\text{xrec}}} \quad \text{Number of detectors per speckle in X-direction}$$

$$Q_y(R) := \frac{S_y(R) \cdot N_{\text{y_pix}}}{D_{\text{yrec}}} \quad \text{Number of detectors per speckle in Y-direction}$$

$$Q(R) := Q_x(R) \cdot Q_y(R) \quad \text{Number of detectors per speckle}$$

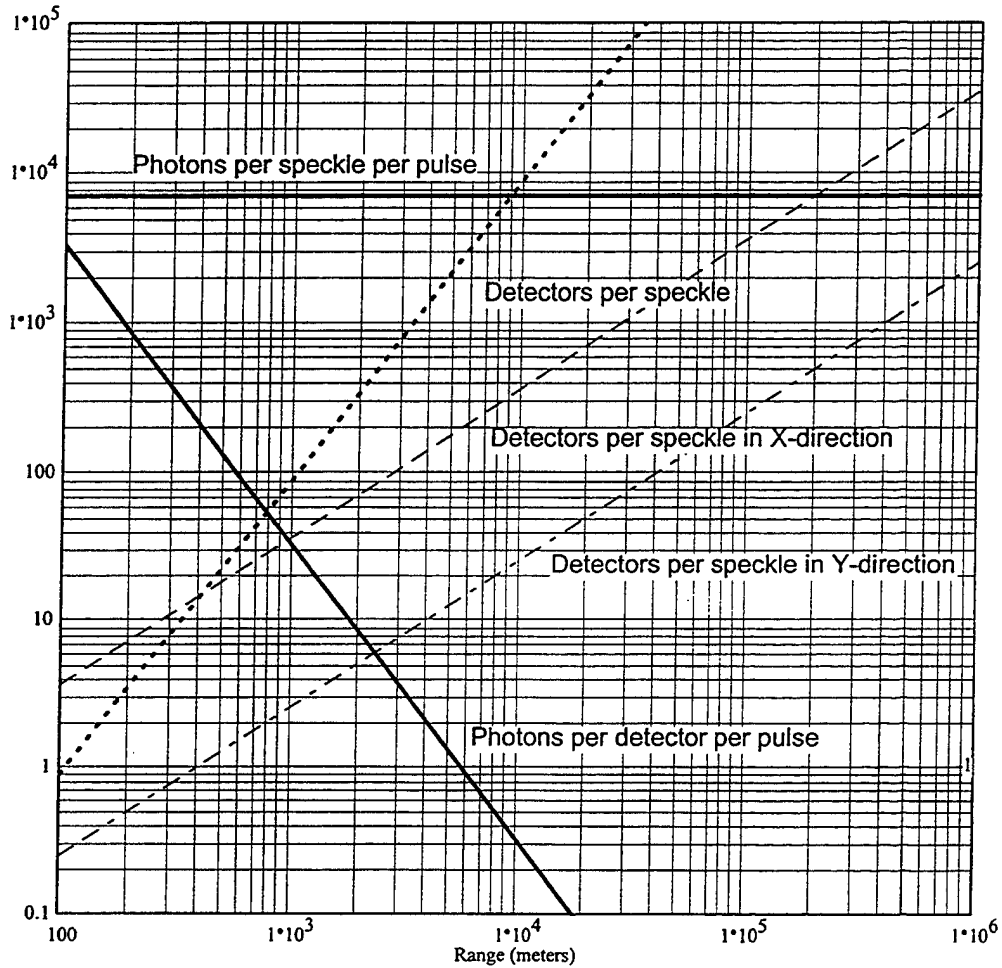
The photons per detector per pulse is given by

$$N_e(R) := \left(\frac{\lambda}{h \cdot c} \right) \cdot \left(\frac{J}{\theta_{tx}(R) \cdot \theta_{ty}(R) \cdot R^2} \right) \cdot \Gamma \cdot \left(\frac{A_{rec}}{4 \cdot \pi \cdot R^2} \right) \cdot \frac{K_{fill}}{N_{x_pix} \cdot N_{y_pix}} \cdot (\eta_{atm}^2 \cdot \eta_{rec} \cdot \eta_{trans} \cdot \eta_{pol})$$

where R is the range to the target.

The number of photons per speckle per pulse is given by

$$N_{spec} := \left(\frac{\lambda}{h \cdot c} \right) \cdot \left[\frac{J}{K_{tx} \cdot L_{tx} \cdot (K_{ty} \cdot L_{ty})} \right] \cdot \rho \cdot \frac{\lambda^2}{\pi} \cdot (\eta_{atm}^2 \cdot \eta_{trans})$$



The calculated parameters for a range of 1 km are:

$$Q_Y(1 \cdot \text{km}) = 2.4603$$

$$N_e(1 \cdot \text{km}) = 32.094$$

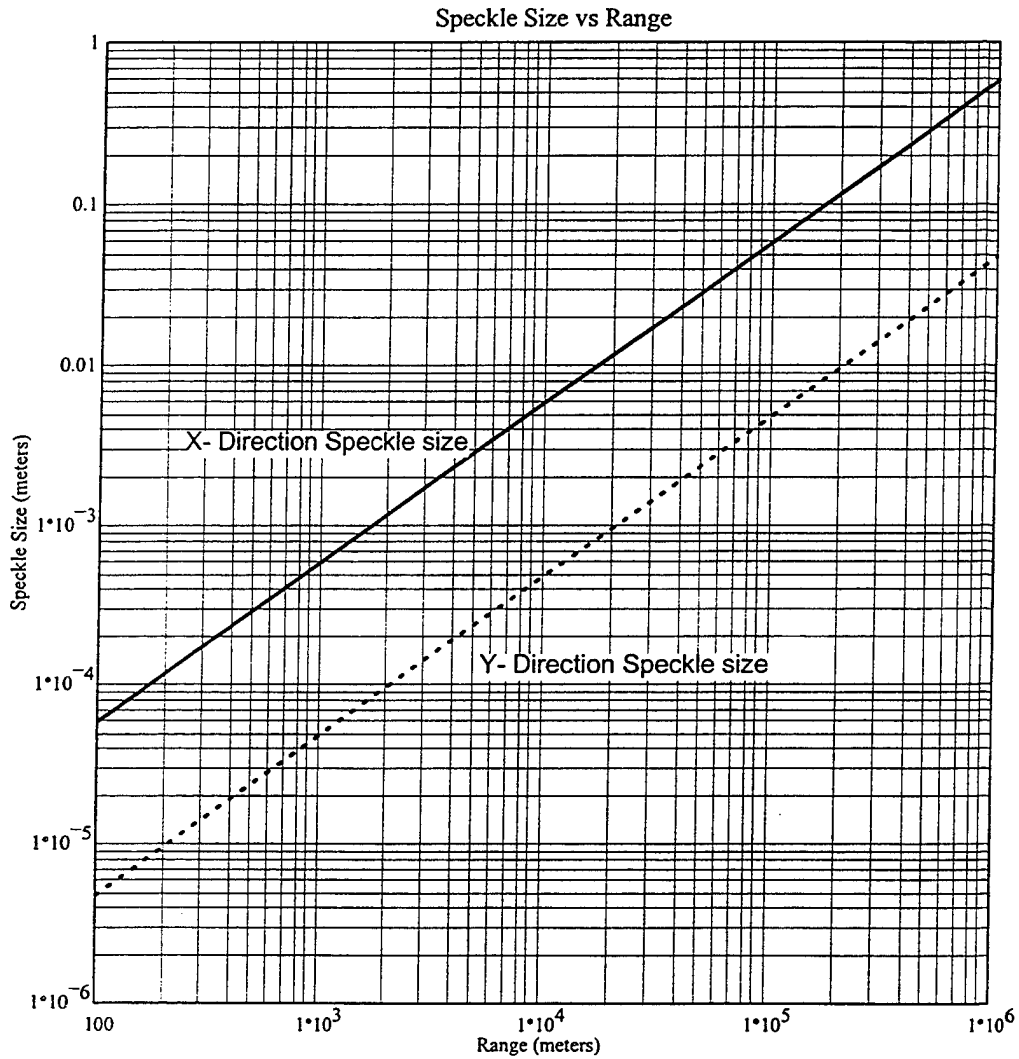
$$Q_X(1 \cdot \text{km}) = 35.41$$

$$N_{spec} = 6.9038 \cdot 10^3$$

$$Q(1 \cdot \text{km}) = 87.1203$$

$$S_x(R) = \frac{\lambda \cdot R}{L_{tx}} \quad \text{X- Direction Speckle size}$$

$$S_y(R) = \frac{\lambda \cdot R}{L_{ty}} \quad \text{Y- Direction Speckle size}$$



The calculated parameters for a range of 1 km are:

$$S_x(1 \cdot \text{km}) = 5.8556 \cdot 10^{-4} \cdot \text{m}$$

$$S_y(1 \cdot \text{km}) = 4.7909 \cdot 10^{-5} \cdot \text{m}$$

$$\frac{D_{xrec}}{S_x(1 \cdot \text{km})} = 21.6888$$

$$\frac{D_{yrec}}{S_y(1 \cdot \text{km})} = 200.3795$$

$$\frac{D_{xrec}}{S_x(1 \cdot \text{km})} \cdot \frac{D_{yrec}}{S_y(1 \cdot \text{km})} = 4.346 \cdot 10^3$$